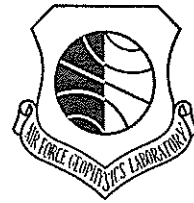


AFGL-TR-79-0210  
INSTRUMENTATION PAPERS, NO. 282



# The Precipitating Electron Detectors (SSJ/3) for the Block 5D/ Flights 2-5 DMSP Satellites: Calibration and Data Presentation

D. A. HARDY, Capt, USAF  
M. S. GUSSENHOVEN  
A. HUBER

14 September 1979

Approved for public release; distribution unlimited.

SPACE PHYSICS DIVISION    PROJECT 7601  
**AIR FORCE GEOPHYSICS LABORATORY**  
HANSCOM AFB, MASSACHUSETTS 01731

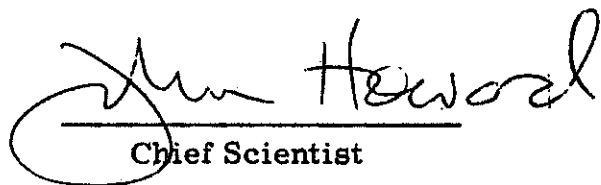
**AIR FORCE SYSTEMS COMMAND, USAF**



This report has been reviewed by the ESD Information Office (OI) and is releasable to the National Technical Information Service (NTIS).

This technical report has been reviewed and is approved for publication.

FOR THE COMMANDER

  
\_\_\_\_\_  
Chief Scientist

Qualified requestors may obtain additional copies from the Defense Documentation Center. All others should apply to the National Technical Information Service.

Unclassified

SECURITY CLASSIFICATION OF THIS PAGE (When Data Entered)

REPORT DOCUMENTATION PAGE		READ INSTRUCTIONS BEFORE COMPLETING FORM
1. REPORT NUMBER AFGL-TR-79-0210	2. GOVT ACCESSION NO.	3. RECIPIENT'S CATALOG NUMBER
4. TITLE (and Subtitle) THE PRECIPITATING ELECTRON DETECTORS (SSJ/3) FOR THE BLOCK 5D/FLIGHTS 2-5 DMSP SATELLITES: CALIBRATION AND DATA PRESENTATION	5. TYPE OF REPORT & PERIOD COVERED Scientific. Interim.	
	6. PERFORMING ORG. REPORT NUMBER	
7. AUTHOR(s) D. A. Hardy, Capt, USAF M. S. Gussenhoven* A. Huber**	8. CONTRACT OR GRANT NUMBER(s)	
9. PERFORMING ORGANIZATION NAME AND ADDRESS Air Force Geophysics Laboratory (PH) Hanscom AFB Massachusetts 01731	10. PROGRAM ELEMENT, PROJECT, TASK AREA & WORK UNIT NUMBERS 62101F 76010812	
11. CONTROLLING OFFICE NAME AND ADDRESS Air Force Geophysics Laboratory (PH) Hanscom AFB Massachusetts 01731	12. REPORT DATE 14 September 1979	
	13. NUMBER OF PAGES 50	
14. MONITORING AGENCY NAME & ADDRESS (if different from Controlling Office)	15. SECURITY CLASS. (of this report) Unclassified	
	15a. DECLASSIFICATION/DOWNGRADING SCHEDULE	
16. DISTRIBUTION STATEMENT (of this Report) Approved for public release; distribution unlimited.		
17. DISTRIBUTION STATEMENT (of the abstract entered in Block 20, if different from Report)		
18. SUPPLEMENTARY NOTES * Boston College, Chestnut Hill, MA ** Emmanuel College, The Fenway, Boston, MA		
19. KEY WORDS (Continue on reverse side if necessary and identify by block number) Aurorae Defense Meteorological Satellite Program (DMSP) Precipitating electrons		
20. ABSTRACT (Continue on reverse side if necessary and identify by block number) In addition to weather monitoring devices, the DMSP satellites currently have on-board auroral imaging devices, precipitating electron detectors, and thermal plasma analyzers. Together these provide a strong tool for analyzing the high latitude, near earth, magnetospheric environment. The program is planned to continue into the 1980s.  The precipitating electrons are measured in 16 energy channels spanning an energy range of 50 eV to 20 keV. The data are routinely processed at the		

Unclassified

SECURITY CLASSIFICATION OF THIS PAGE(When Data Entered)

20. Abstract (Continued)

Air Force Geophysics Laboratory and have the potential of providing real-time monitoring of auroral activity through oval boundary measurements.

To facilitate the use of these data and to examine the feasibility of making consistent, reliable boundary measurements, this report has been prepared. It contains the following: 1) A general description of the DMSP-F2 orbit, its variations in universal time and season, and the pertinence of these variations to boundary measurements. 2) A description of the SSJ/3 package, one of which is built for each of four DMSP satellites and the results of calibrating two of the instruments. 3) A discussion of the way the data is processed at the Air Force Geophysics Laboratories. 4) A comparison of Northpole-Southpole passes during a magnetospherically quiet period and during an active period, and a discussion of the general features of the electron precipitation as they may be used to determine auroral boundaries.

Unclassified

SECURITY CLASSIFICATION OF THIS PAGE(When Data Entered)

## Contents

1. INTRODUCTION	7
2. THE DMSP-F2 ORBIT	10
3. DESCRIPTION OF THE EXPERIMENT AND CALIBRATION RESULTS	15
4. DATA REDUCTION OF SSJ/3 ON DMSP-F2 AS PERFORMED AT AFGL	31
5. EXAMINATION OF DATA FROM FOUR PASSES	39
5.1 North Pole Active: 28 February 1978	40
5.1.1 Evening Equatorward	40
5.1.2 Evening Poleward	41
5.1.3 Morning Equatorward	41
5.1.4 Morning Poleward	41
5.2 South Pole Active: 28 February 1978	41
5.2.1 Evening Equatorward	41
5.2.2 Evening Poleward	42
5.2.3 Morning Equatorward	43
5.2.4 Morning Poleward	43
5.3 Some Comments on the Active Cases	43
5.4 North Pole Quiet: 21 January 1978	44
5.5 South Pole Quiet: 21 January 1978	46
6. CONCLUSION	46
REFERENCES	49

## Illustrations

1. The DMSP-F2 Satellite Paths Over the North Polar Regions for Given Universal Times, Plotted in Corrected Geomagnetic Latitude and Magnetic Local Time. (Data taken from February 1978 passes)	11
2. The DMSP-F2 Satellite Paths Over the South Polar Regions for Given Universal Times, Plotted in Corrected Geomagnetic Latitude and Magnetic Local Time. (Data taken from February 1978 passes)	11
3. The Seasonal Dependence of the DMSP-F2 Satellite Path Between 06-07 UT Over the North Polar Region (Plotted in Corrected Geomagnetic Latitude and Magnetic Local Time)	12
4. A Double-dash Line Representation of the Quiet Time Auroral Oval (A Circle Offset from the Geomagnetic Pole $4^\circ$ Toward Midnight and of Radius $20^\circ$ , Superposed on the North Polar Satellite Paths of DMSP-F2, Plotted in Corrected Geomagnetic Latitude and Magnetic Local Time, as Shown in Figure 1)	12
5. The Universal Time Variation in the Morning Equatorward Auroral Boundary That Would be Measured by DMSP-F2 if the Equatorward Oval Boundary were a Circle Offset from the Geomagnetic Pole $4^\circ$ Toward Midnight and of Radius $20^\circ$	13
6. The Universal Time Variation in the Evening Equatorward Auroral Boundary That Would be Measured by DMSP-F2 if the Equatorward Oval Boundary were a Circle Offset from the Geomagnetic Pole $4^\circ$ Toward Midnight and of Radius $20^\circ$	14
7. The Angular Response of Detector 4 in Channel 8 to a Beam with an Energy of 985 eV	16
8a. The Energy Dependent Geometric Factor, $G(E)$ , Plotted as a Function of Energy for Channel 8 of Detectors 4 and 5	17
8b. The Energy Dependent Geometric Factor, $G(E)$ , Plotted as a Function of Energy for Channel 9 of Detectors 4 and 5	18
9. Details of the Configuration of the Apertures and Curved Plates of the Analyzer Showing the Angles $\alpha$ and $\beta$	20
10. Angular Response of Detectors 4 and 5 on Channel 8	21
11. Angular Response of Detectors 4 and 5 on Channel 9	22
12. The Energy Dependent Geometric Factor, $G(E)$ , Normalized to the Peak Geometric Factor, $G_0(E_0)$ , Plotted as a Function of Energy Normalized to the Channels Central Energy, $E_0$ . The figure shows the data from channels 9 through 12 for Detector 5	25
13. The Energy Dependent Geometric Factor, $G(E)$ , Normalized to the Peak Geometric Factor, $G_0(E_0)$ , Plotted as a Function of Energy Normalized to the Channels Central Energy, $E_0$ . The figure shows the data from channels 9 through 12 for Detector 4	26

## Illustrations

14. Normalized Curves of the Energy Dependent Geometric Factor as in Figure 12 for Channels 1 through 4 of Detector 4	27
15. Normalized Curves of the Energy Dependent Geometric Factor as in Figure 12 for Channels 5 through 8 of Detector 4	28
16. Normalized Curves of the Energy Dependent Geometric Factor as in Figure 12 for Channels 1 through 4 of Detector 5	29
17. Normalized Curves of the Energy Dependent Geometric Factor as in Figure 12 for Channels 5 through 8 of Detector 5	30
18. The Format in Which the DMSP-F2 Precipitating Electron Data is Processed	33
19. Same as Figure 18, but for a Later UT in Which the Satellite Path Does Not Enter the North Polar Cap, but Passes Through the Midnight Oval	34
20. Same as Figure 18, but for a Later UT in Which the Satellite Path Does Not Enter the South Polar Cap, but Passes Through the Midday Oval, or the Cusp Region	35
21. Same as Figure 20, but for a Later UT in Which the Satellite Path is Always Equatorward of the Midday Oval	36
22. The DMSP-F2 Image for 3 January 1978, Near 15 UT Gridded in Corrected Geomagnetic Coordinates	37
23. The Precipitating Electron Data for the DMSP-F2 Pass on 3 January 1978, Near 15 UT (Whose Auroral Image is Shown in Figure 22)	38
24. Ten Differential Energy Spectra for Ten Successive Seconds of DMSP-F2 Precipitating Electron Data Taken on 3 January 1978 at 15-18-5 to 15-18-14 UT	39
25. DMSP-F2 Precipitating Electron Data for a North Polar Pass During High Magnetic Activity	40
26. DMSP-F2 Precipitating Electron Data for a South Polar Pass During High Magnetic Activity	42
27. DMSP-F2 Precipitating Electron Data for a North Polar Pass During Low Magnetic Activity	44
28. DMSP-F2 Precipitating Electron Data for a South Polar Pass During Low Magnetic Activity	45
29. Summary of the Oval Size for Active and Quiet Magnetic Conditions as Determined from the Poleward and Equatorward Boundaries in Figures 25 to 28	47

## Tables

1. Calibration Figures for Detectors 4 and 5	23
2. Channeltron Efficiency	24
3. Comparison of Geometric Factors Derived for Detectors 2 and 3 and Those Derived for Detectors 4 and 5	31



# The Precipitating Electron Detectors (SSJ/3) for the Block 5D/Flights 2-5 DMSP Satellites: Calibration and Data Presentation

## 1. INTRODUCTION

The Defense Meteorological Satellite Program (DMSP) of the U.S. Air Force is now projected to continue well into the 1980s. The Program calls for two satellites to be in polar orbit at all times: one in the dawn-dusk meridian and one in the noon-midnight meridian. Depending on launch dates and system lifetimes there can be as many as three or as few as one satellite in operation at a given time. The Program is principally devoted to weather monitoring but radiometers operating over darkened areas produce the now familiar images of the auroral regions. These images provided the first extended views of auroral phenomena, and are available from 1971 to the present.

Since 1974, low-energy electron analyzers have been placed on dawn-dusk satellites in the Program. The satellites are non-spinning and the detectors are positioned to measure precipitating electrons. The original electrostatic analyzers measured electrons in six channels from 0.2 to 20 keV. Since July 1977, with the launch of DMSP-F2, these have been replaced by a set of two electrostatic analyzers on board covering the range 50 eV to 20 keV in 16 energy channels. An identical package was also flown on the F-3 satellite and additional instruments will be on DMSP F4 and F5 (dawn-dusk and noon-midnight orbits) which have yet to be launched. With DMSP F6, F7 and F8 additional electrostatic analyzers will be

(Received for publication 13 September 1979)

included to measure the flux of precipitating protons. Together with the imaging devices, the improved measurements of precipitating electrons will continue to give this Program a central place in the continuing understanding of auroral and polar cap phenomena, and their relation to magnetospheric dynamics.

The spatial extent and small-scale resolution of the DMSP images has greatly increased the accuracy with which large numbers of researchers can visualize auroral activity. One now commonly makes reference to an "instantaneous" auroral oval since large portions of the auroral zone can often be seen on a single DMSP image. Because of the considerable influence of the images on auroral research and because they continue to be routinely made, considerable effort has gone into the calibration of the sensitivity of the images to incorporate them accurately into the body of other past and future auroral measurements (Mizera et al,<sup>1</sup> Mende and Eather,<sup>2</sup> and Eather<sup>3</sup>). For similar reasons we have prepared this report on the current and projected precipitating electron measurements made by DMSP. These data are available in raw count form from the World Data Center. In addition, all the data is processed in the manner we report here at the Air Force Geophysics Laboratory.

It should also be noted that the auroral visual and particle data from DMSP may be supplemented with simultaneous measurements of the ionospheric thermal plasma by the SSIE instrument (Smiddy et al<sup>4</sup>). This instrument was designed to measure the mass, density and temperature of the thermal ions as well as the density and temperature of the thermal electrons. Outputs are used by Air Weather Service to provide F region scale heights for global ionospheric modelling. Obviously, comparisons of simultaneous SSIE and SSJ/3 measurements can be exploited to provide unique information for modelling the dynamic response of the ionosphere to directly measured inputs from energetic particles.

The current measurements of precipitating electrons appear to be of such consistently high quality that their use to monitor the auroral regions on a real time basis is an obvious and important use of the data, particularly with the long time delay before A-indices are available. For this reason we will focus on the problems of obtaining consistent, meaningful auroral boundaries from the data.

- 
1. Mizera, P.F., Croley, Jr., D.R., Morse, F.A., and Vampola, A.L. (1975) Electron fluxes and correlations with quiet time auroral arcs, J. Geophys. Res. 80:2129.
  2. Mende, S.B. and Eather, R.H. (1976) Monochromatic all-sky observations and auroral precipitation patterns, J. Geophys. Res. 81:3771.
  3. Eather, R.H. (1979) DMSP Calibration, J. Geophys. Res. 84:4134.
  4. Smiddy, M., Sagalyn, R.C., Sullivan, W.P., Wildman, P.J.L., Anderson, P., and Rich, F. (1978) The Topside Ionosphere Plasma Monitor (SSIE) for the Block 5D/Flight 2 DMSP Satellite, AFGL-TR-78-0071, AD A058 503.

The quantity of data also makes possible accurate statistical surveys of particular features of auroral activity and their relation to interplanetary and magnetospheric conditions. Earlier DMSP electron data have been used by Meng et al<sup>5</sup> and Meng and Kroehl<sup>6</sup> to show correlations between the direction of the interplanetary magnetic field and differences in fluxes both between polar caps and dawn-to-dusk in a single cap. (See also the review by Mizera and Fennel<sup>7</sup> for contributions from the Isis satellites.)

Other detectors on spinning satellites have necessarily sacrificed time resolution for pitch angle distributions. DMSP satellites, since they are nonspinning, have excellent time resolution, but no resolution in pitch angle. The DMSP satellite data can provide, therefore, an extension to the many interesting types of events recorded by other satellites, such as the intense keV fluxes in the caps reported by Foster and Burrows<sup>8</sup> to occur after major storms. Additionally, any case study of events in the magnetosphere can have as an additional environmental input the state of the auroral and cap regions as determined by the DMSP images and the precipitating electrons.

This report, then, contains the following:

1. A general description of the orbit of the DMSP-F2, the currently orbiting satellite.
2. A description of the SSJ/3 package, one of which is built for each of the F2, F3, F4, F5 satellites, and the results of calibrating the last two instruments. These calibrations are compared to the previous calibrations of the first two instruments.
3. A discussion of the way the data are processed at the Air Force Geophysics Laboratories.
4. A comparison of North Pole-South Pole passes during a magnetospherically quiet period and during an active period, and a discussion of the general features of the electron precipitation particularly for the purpose of determining auroral boundaries.

- 
5. Meng, C.-I., Holzworth, R.H., and Akasofu, S.-I. (1977) Auroral circle-delineating the poleward boundary of the quiet auroral belt, J. Geophys. Res. 82:164.
  6. Meng, C.-I. and Kroehl, H.W. (1977) Intense uniform precipitation of low-energy electrons over the polar cap, J. Geophys. Res. 82:2305.
  7. Mizera, P.F. and Fennell, J.F. (1978) Satellite observations of polar, magnetotail lobe, and interplanetary electrons at low energies, Rev. Geophys. Space Phys. 16:147.
  8. Foster, J.C. and Burrows, J.R. (1976) Electron fluxes over the polar cap, 1, intense keV fluxes during poststorm quieting, J. Geophys. Res. 81:6016.

## 2. THE DMSP-F2 ORBIT

DMSP-F2 was launched into a circular polar orbit in July 1977. The orbit has an inclination of  $99^\circ$ , an altitude of 830 km and a period of 101 min. It is sun-synchronous and remains throughout its lifetime at the same inclination of  $9^\circ$  from the geographic poles and in the dawn-to-dusk plane. Since the magnetic poles rotate about the geographic poles, the F2 orbit changes systematically in geomagnetic coordinates throughout a 24-hour period.

Summaries of the satellite paths over the north and south polar regions throughout Day 59, 1978 (Feb. 28) are given in Figures 1 and 2. The south polar plots are similar to those given by Candidi et al.<sup>9</sup> The paths have been projected along magnetic field lines to 100 km using a Jensen-Cain model of the magnetic field; the corrected geomagnetic latitudes of the projections are plotted as a function of magnetic local time. The paths are drawn across the magnetic latitude interval  $70^\circ$ - $90^\circ$  for both poles. Each line represents the path for the approximate UT listed at the side, starting at the beginning of the day. The areas of cross-hatching represent a group of paths for the time interval listed.

For a broad time interval ( $\sim 0:00$ - $11:00$  UT) the subsatellite path falls across the polar cap in both polar regions, varying in geomagnetic local time from 1800-2100 at  $70^\circ$  in the evening (dusk), and 5:30-8:30 at  $70^\circ$  in the morning (dawn). For universal times greater than 11:00 UT the north polar satellite path will not reach geomagnetic latitudes greater than  $80^\circ$  and will lie at latitudes, for the most part, in the midnight sector "instantaneous" oval. The same is true for the south polar region except that satellite paths for times greater than 11:00 UT are in the midday sector at cusp latitudes and below.

The satellite orbits are constant in UT over the life of the satellite in geographic and, therefore, geomagnetic coordinates. However, since we are interested in the orbit description in geomagnetic latitude and magnetic local time there will be a seasonal rotation of the orbits because of the seasonal dependence of magnetic local time (Whalen<sup>10</sup>). Figure 3 shows the rotation for winter, spring, summer and fall seasons. The maximum rotation is approximately 40 minutes. The polar cap coverage remains essentially the same throughout the satellite lifetime. (Note: The F2 is anomalous in that it drifts slowly in local time changing by approximately one hour per year.)

- 
9. Candidi, M., Kroehl, H.W., Kosinski, G., and Buhmann, R.W. (1978) DMSP-F2 observations of cusplike electron precipitation regions during the September 19-21, 1977 event, Space. Sci. Rev. 22:667.
  10. Whalen, James A. (1970) Auroral Oval Plotter and Nomograph for Determining Corrected Geomagnetic Local Time, Latitude and Longitude for High Latitudes in the Northern Hemisphere, AFCRL-70-0422, AD 713 170.

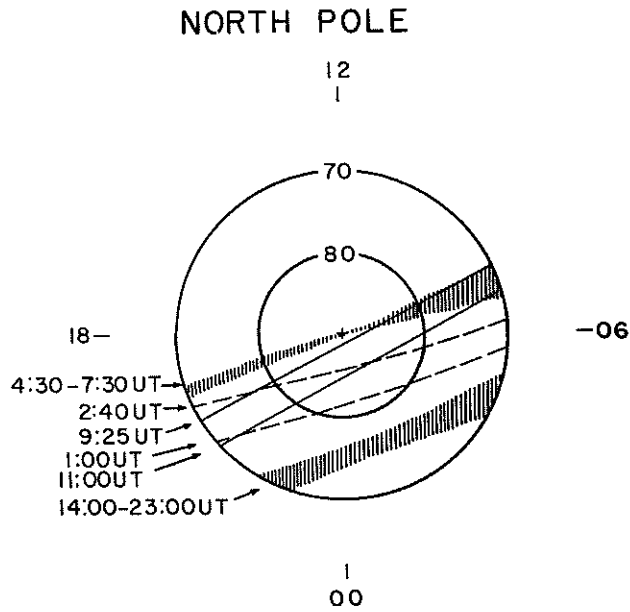


Figure 1. The DMSP-F2 Satellite Paths Over the North Polar Regions for Given Universal Times, Plotted in Corrected Geomagnetic Latitude and Magnetic Local Time. (Data taken from February 1978 passes)

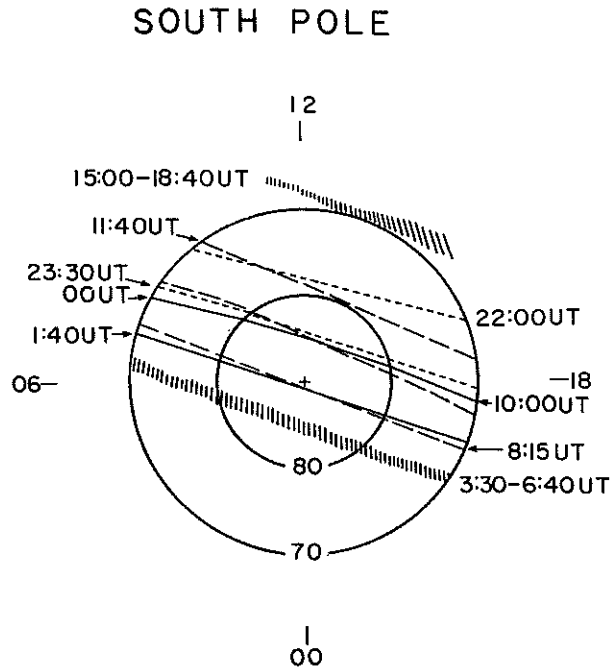


Figure 2. The DMSP-F2 Satellite Paths Over the South Polar Regions for Given Universal Times, Plotted in Corrected Geomagnetic Latitude and Magnetic Local Time. (Data taken from February 1978 passes)

NORTH POLE

12

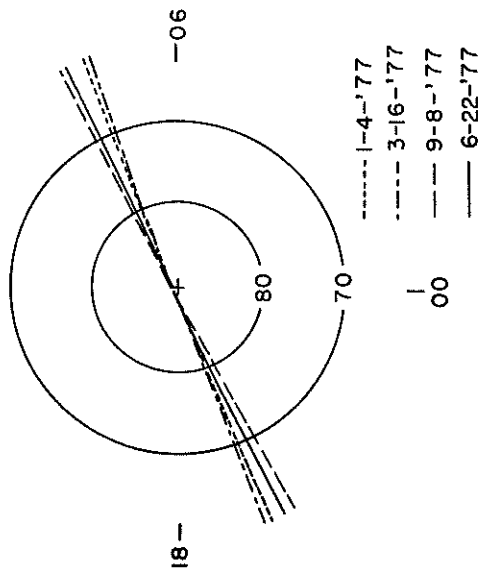


Figure 3. The Seasonal Dependence of the DMSP-F2 Satellite Path Between 06-07 UT Over the North Polar Region (Plotted in Corrected Geomagnetic Latitude and Magnetic Local Time). The days for which the data are taken are shown in the legend

NORTH POLE

12

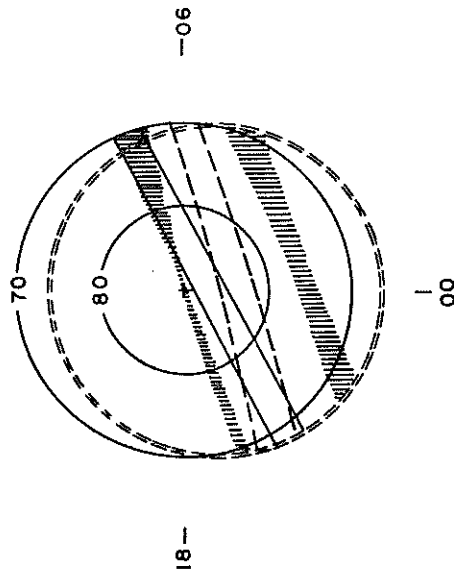


Figure 4. A Double-dash Line Representation of the Quiet Time Auroral Oval (A Circle Offset from the Geomagnetic Pole 4° Toward Midnight and of Radius 20°, Superposed on the North Polar Satellite Paths of DMSP-F2, Plotted in Corrected Geomagnetic Latitude and Magnetic Local Time, as Shown in Figure 1)

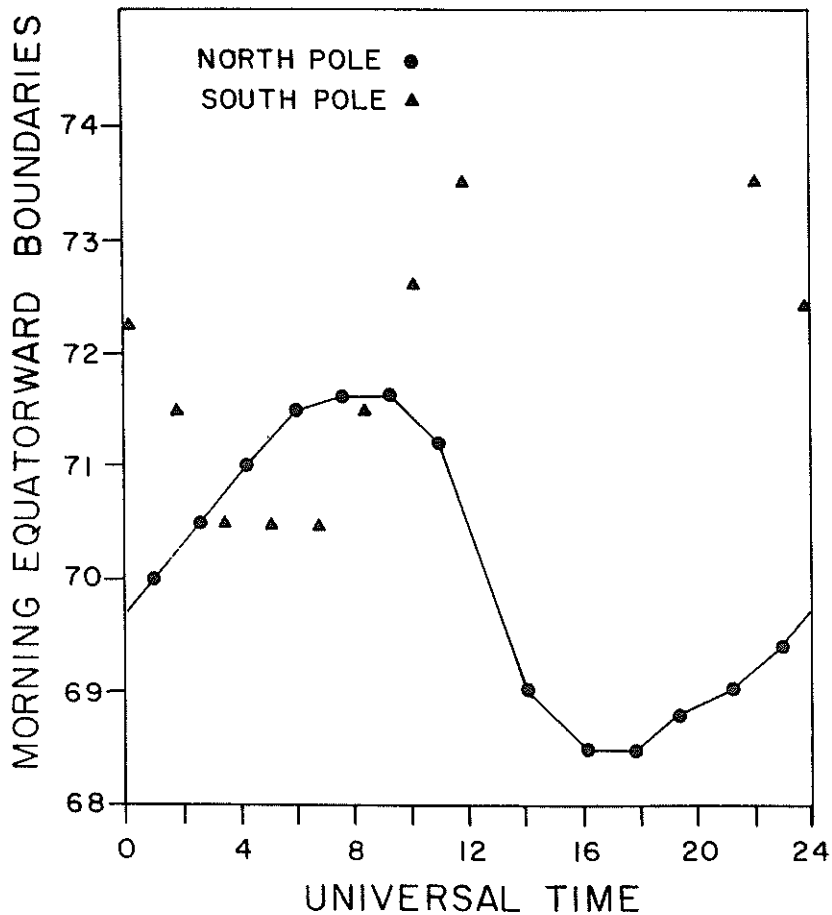


Figure 5. The Universal Time Variation in the Morning Equatorward Auroral Boundary that would be Measured by DMSP-F2 if the Equatorward Oval Boundary were a Circle Offset from the Geomagnetic Pole  $4^{\circ}$  Toward Midnight and of Radius  $20^{\circ}$ . The connected dots show variations for the North Pole equatorward boundary, and the triangles for the South Pole

The dawn-dusk series of DMSP satellites appear to be particularly useful satellites to determine auroral boundaries since two equatorward boundaries are crossed in a given pole every 100 minutes. However, equatorward boundaries, even for a given magnetic activity are known to be asymmetric in local time. In fact, Meng et al<sup>5</sup> and Rossberg<sup>11</sup> find that for quiet times the best representation of the auroral oval is a circle whose center is offset from the magnetic pole toward the midnight sector by about  $4^{\circ}$ . This asymmetry will lead to a universal time variation in boundary measurements even though there is, in fact, no change in the

11. Rossberg, L. (1978) Undisturbed trapping boundary for energetic electrons at low altitudes, *J. Geophys. Res.* 83:4307.

oval. To show this we superimposed in Figure 4 an offset circle (offset by  $4^\circ$  toward midnight) of radius  $20^\circ$  on a north polar cap with the DMSP-F2 orbits of Figure 1. The intersections of the paths with the offset circle will constitute the equatorward edge of the oval. These positions are plotted in Figures 5 and 6 for dawn and dusk boundaries. The circles connected with a line are for the North Pole; the triangles are for similar positions in the South Pole. There is, of course, a variation in equatorward edge of nearly  $4^\circ$  since most of the offset will be realized in the dawn and dusk regions.

Thus, it cannot be too firmly stressed that any attempt to use DMSP Satellite auroral boundaries (or those from any other satellite) to determine the state of the high latitude regions must, for any kind of consistency, take into account the local time variation of the oval boundaries for given magnetic activities.

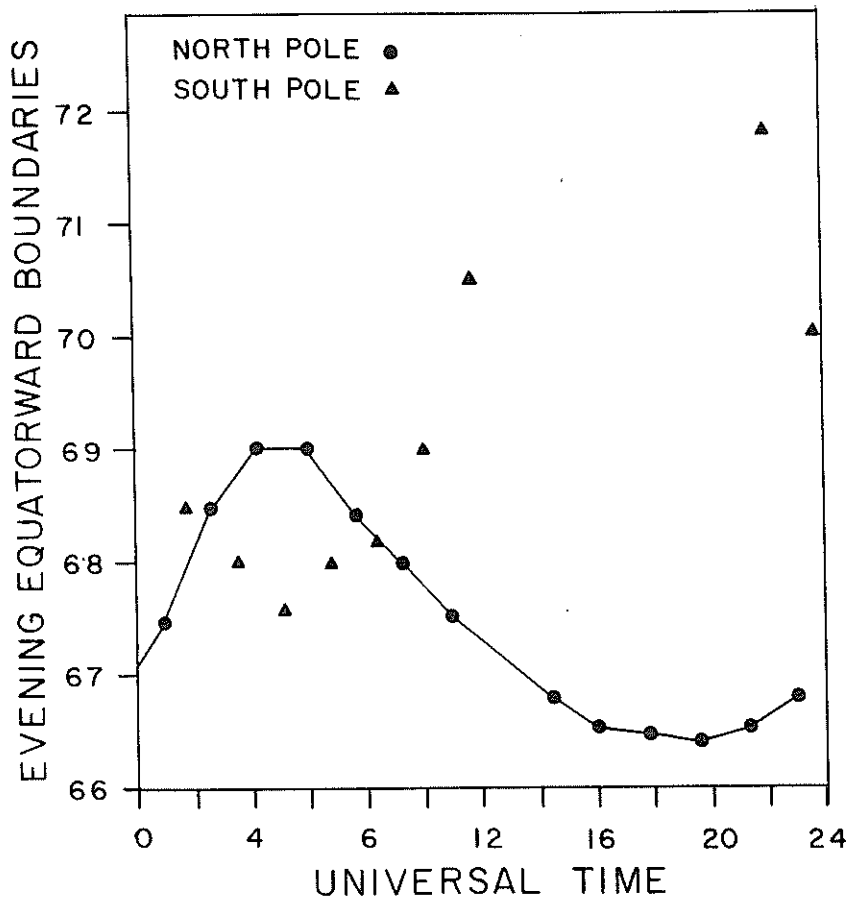


Figure 6. The Universal Time Variation in the Evening Equatorward Auroral Boundary that would be Measured by DMSP-F2 if the Equatorward Oval Boundary were a Circle Offset from the Geomagnetic Pole  $4^\circ$  Toward Midnight and of Radius  $20^\circ$ . The connected dots show variations for the North Pole equatorward boundary, and the triangles for the South Pole



### 3. DESCRIPTION OF THE EXPERIMENT AND CALIBRATION RESULTS

The first four SSJ/3 detectors to be flown on the F2, F3, F4 and F5 satellites are identical in design. They are built to measure the flux of electrons incident to the spacecraft in 16 energy bins spanning in energy from 50 eV to 20,000 eV. This is accomplished using two sets of curved plates that are sequenced through 8 voltage levels in tandem each second. The detector dwells for a period of 98 milliseconds in each channel with 2 milliseconds being left between steps to stabilize the voltage. The plates sequence from high voltage to low and after the 8th level the detector holds for 200 milliseconds before restarting the sequence.

The DMSP satellites are non-spinning. The SSJ/3 sensors are mounted on the satellite such that their look direction is oriented radially outward from the earth at all times. The total package weighs 3.046 lbs and consumes 0.125 watts of power.

The first two detectors were calibrated using Monte Carlo techniques and limited analysis with a beam system. This work has been reported on previously (Huber et al.<sup>12</sup>). The third and fourth detectors (on F4 and F5) were calibrated using an electron beam system at Rice University in Houston, Texas. The calibration results of the third and fourth detectors are reported here even though the geometric factors obtained by Huber are used in the data reduction for F2 currently in orbit. We feel that comparison of the earlier calibration results with the more extensive method used here will at least verify to a specified accuracy the earlier calibrations, and may present possible corrections to the geometric factors now used.

The electron beam system consists of an aluminum plate irradiated by a set of UV lamps. The photoelectrons driven off the plate by the UV are accelerated by a series of grids between the plate and the detector to be calibrated. The instrument to be calibrated is mounted on a fixture such that the look direction of the detector can be positioned at any angle desired relative to the beam. The system produced a homogeneous beam of electrons with an ~18 inch radius. The energy of the beam is turnable in energy from approximately 30 volts to 35,000 volts. The entire system is contained within a set of Hemholz coils used to cancel out the earth's magnetic field.

The calibration system is computer controlled such that it automatically sequences through a two dimensional array of angles relative to the detector aperture for any fixed energy of the incident beam. The counts accumulated as the detector dwells at each angular position are stored in core and recorded onto magnetic tape.

---

12. Huber, A., Pantazis, J., Besse, A. L., and Rothwell, P. L. (1977)  
Calibration of the SSJ/3 Sensor on the DMSP Satellites, AFGL-TR-77-0202, AD A045 997.

The current density in the beam is determined using a Faraday cup that is shifted into the beam at the beginning of each angular scan. The counts observed over a typical angular scan are shown in Figure 7.

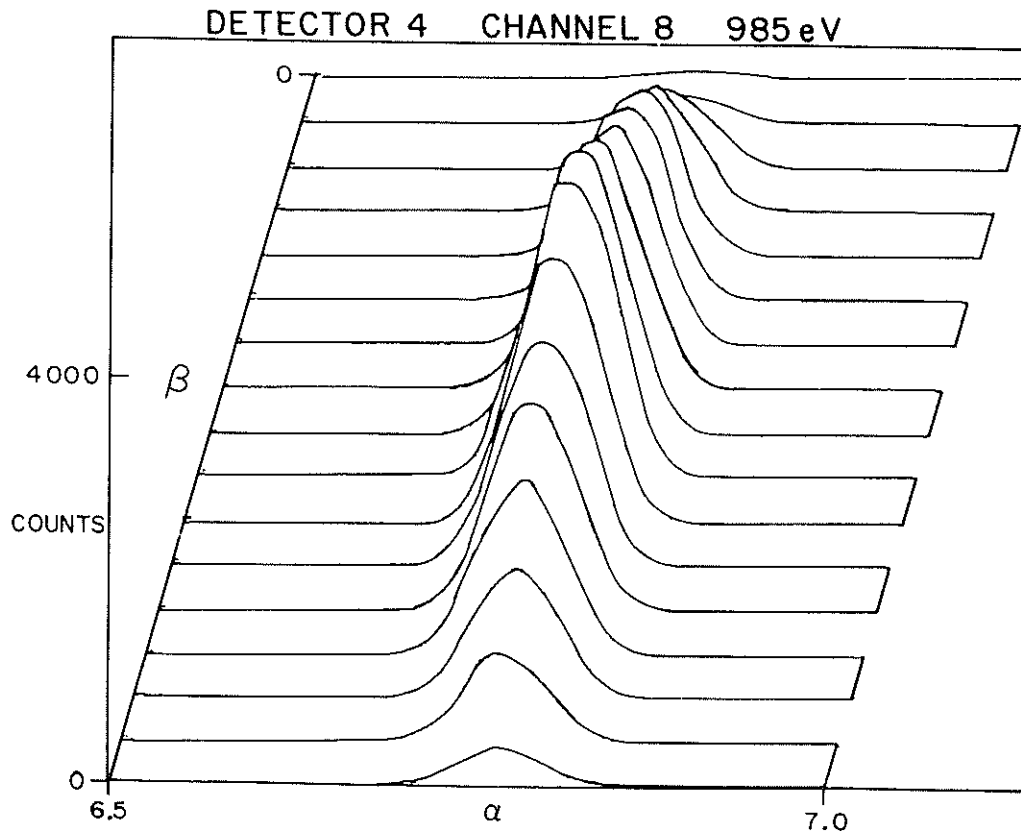


Figure 7. The Angular Response of Detector 4 in Channel 8 to a Beam with an Energy of 985 eV. The angles  $\alpha$  and  $\beta$  are measured in two orthogonal directions relative to the normal to the detector aperture

At the end of each scan the computer calculates the energy dependent geometric factor,  $G(E)$ . By determining  $G(E)$  at a series of energies one can approximate the response curve for each fixed voltage on the plates. The response curve allows one to determine the channel pass band,  $\Delta E$ , and by integrating over the response curve one can calculate the energy independent geometric factor  $G$ .  $G$  is defined such that

$$j(E) = \frac{C/\Delta T}{G} \quad (1)$$

where  $j(E)$  is the differential flux (electrons/cm<sup>2</sup>-sec ster. -eV) in the channel with central energy  $E$ ,  $C$  is the count observed in that channel, and  $\Delta T$  is the accumulation interval for these counts.  $G$  is given in units of cm<sup>2</sup>-ster. -eV.

In the Rice calibration, the SSJ/3 detectors for the F-4 and F-5 satellites were mounted in the chamber together, with the Faraday cup in between the two detectors. Approximately two hundred angular scans were made to map the response curves for the sixteen channels. In Figures 8a and 8b the representative response curves are shown. Each plot contains the response curves from both detectors.

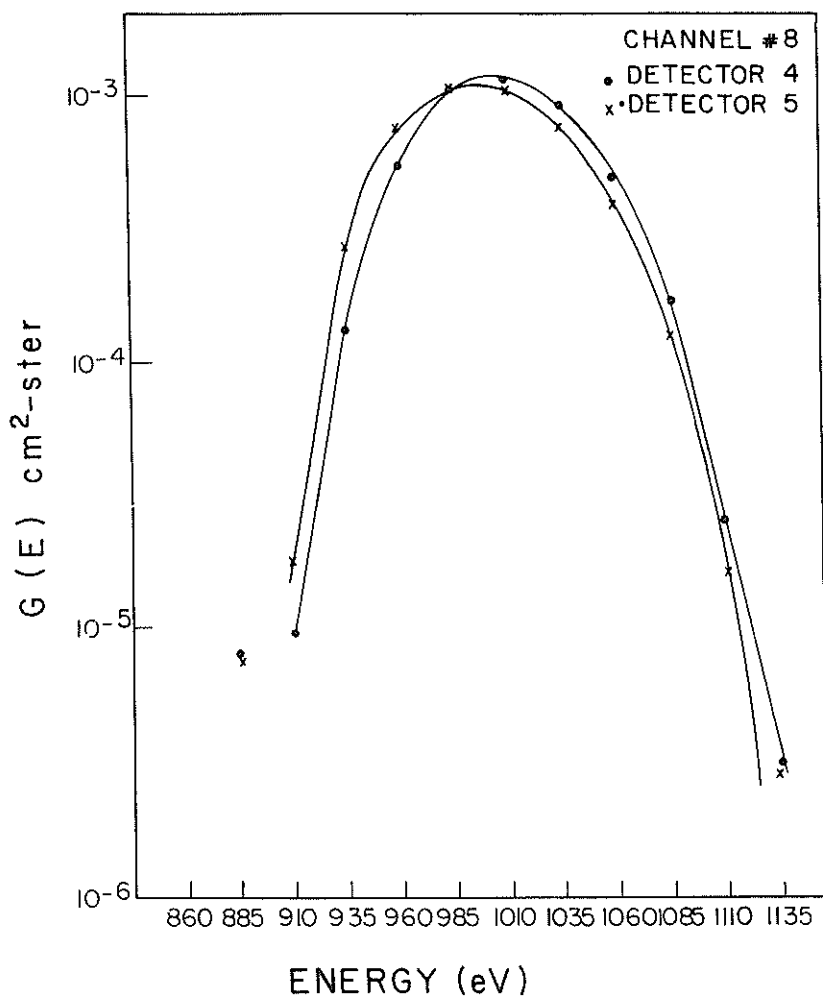


Figure 8a. The Energy Dependent Geometric Factor,  $G(E)$ , Plotted as a Function of Energy for Channel 8 of Detectors 4 and 5

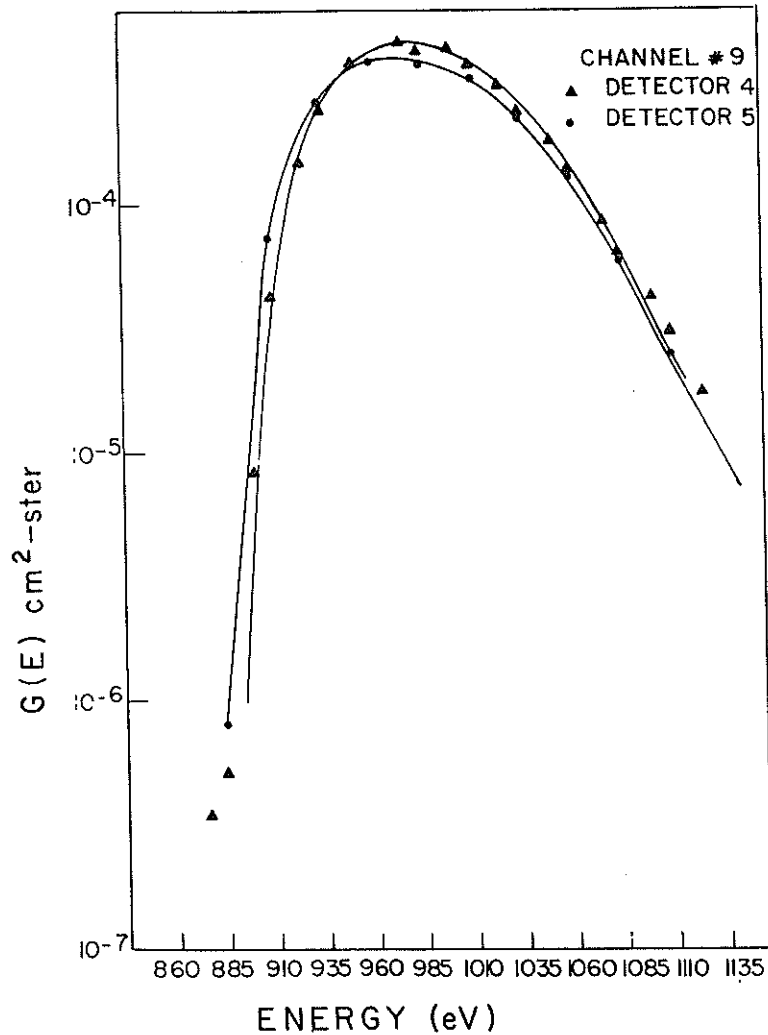


Figure 8b. The Energy Dependent Geometric Factor, G(E), Plotted as a Function of Energy for Channel 9 of Detectors 4 and 5

In the following we will refer to detectors 4 and 5 depending on whether we are considering the detector for the F-4 or F-5 satellites respectively. Notice that for channel 8 the results from the two detectors are in excellent agreement. The central energies agree to within 1 percent and the peak values of G(E) to within 6 percent. The shapes of the response curves are almost identical. For channel 9 the agreement is not quite as good. In this case the peak values of G(E) differ by approximately 15 percent ( $4.5 \times 10^{-4}$  for detector 4 as opposed to  $3.8 \times 10^{-4}$  for detector 5) and the width of the response curves also differ ( $\Delta E/E$  of 0.10 as

opposed to 0.131 for detectors 4 and 5 respectively). The reason for the difference is not understood at present.

The angular resolution of the detectors was determined by looking at the response of channels 8 and 9 at approximately their central energies in directions perpendicular and parallel to the two cylindrical plates of the analyzer. The two angles  $\alpha$  and  $\beta$  are shown in Figure 9 and the response curves for variations in both angles are shown in Figures 10 and 11. In the figures the response has been normalized to the counts observed where  $\alpha = \beta = 0$ .  $\Delta\alpha$  and  $\Delta\beta$  are defined as the full width at half maximum of the angular response. The values for  $\Delta\alpha$  and  $\Delta\beta$  for the two detectors are:

$\Delta\alpha$ (Channel 8)		$\Delta\alpha$ (Channel 9)	
Detector 4	Detector 5	Detector 4	Detector 5
2.0°	1.8°	3.85°	3.50°
$\Delta\beta$ (Channel 8)		$\Delta\beta$ (Channel 9)	
Detector 4	Detector 5	Detector 4	Detector 5
10.45°	8.8°	4.60°	4.60°

The two detectors are in close agreement except for  $\Delta\beta$  in Channel 8 where the two detectors differ by approximately 15 percent.

For channels 1 through 8 the calibration gave excellent results. In Table 1 the peak energy, the full width at half maximum, the peak value of  $G(E)$  and the integrated energy independent geometric factor for each channel are listed. The peak value of  $G(E)$  decreases with increasing energies from a value of approximately  $1.1 \times 10^{-3}$  at 1 KeV to  $\sim 8 \times 10^{-4}$  at 20 KeV. This arises from a decrease in channeltron efficiency with increasing energy.

It is important to compare the observed decrease in channeltron efficiency to that predicted from the work of Archuleta and DeForest.<sup>13</sup> They maintain that the efficiency of a channel electron multiplier between 1 KeV and 50 MeV has a functional form

$$\epsilon = 1.0 - \frac{2.0}{\left[ 3.0 + \frac{6.5}{(E + 0.05)} + \frac{30}{(E + 0.05)^3} \right]} \quad (2)$$

13. Archuleta, R.J. and DeForest, S.E. (1971) Efficiency of channel electron multipliers for electrons of 1-50 keV, Rev. of Sci. Instru. 42:89.

## SSJ/3 ESA ASSEMBLY

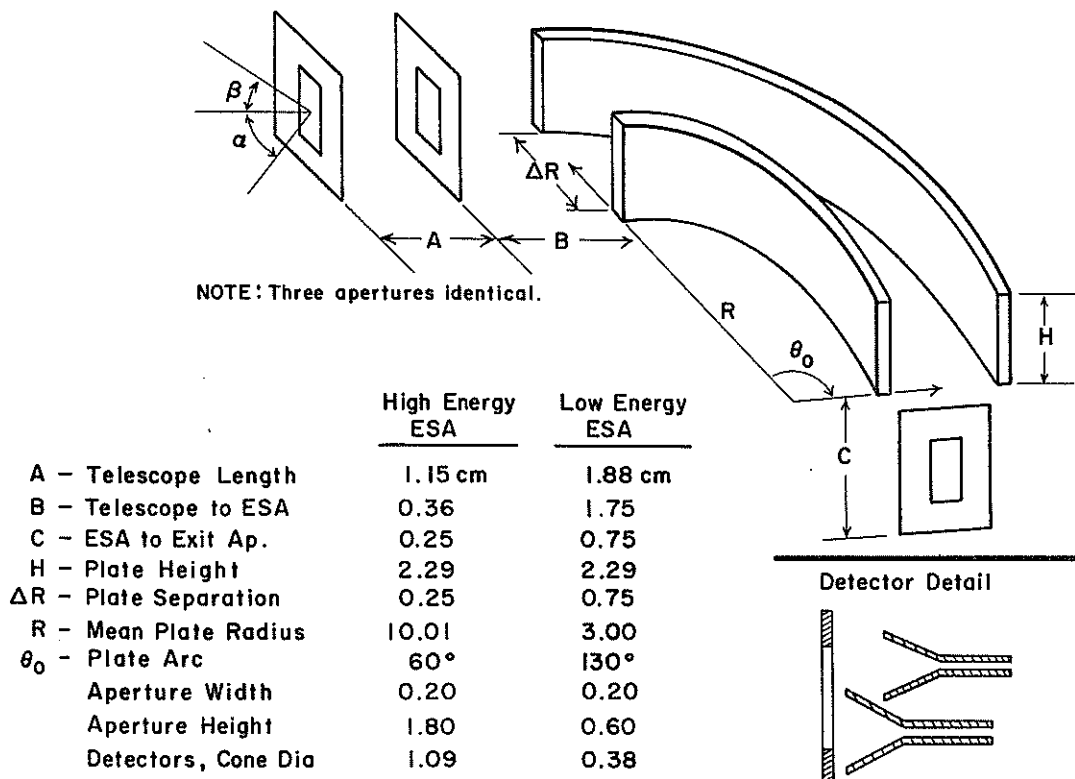


Figure 9. Details of the Configuration of the Apertures and Curved Plates of the Analyzer Showing the Angles  $\alpha$  and  $\beta$

where E is expressed in KeV. We have found the shape of the response curve to remain the same for all the channels above 1 KeV. The decrease in the peak value we attribute, therefore, exclusively to a change in channeltron efficiency. We assume the efficiency in channel 8 is unity and have taken the ratio of the peak value of G(E) in preceding channels to the peak value of G(E) in channel 8 to give the efficiency. In Table 2 we have listed the efficiencies determined in this manner together with the values predicted from Eq. (2). One notes that in the energy range

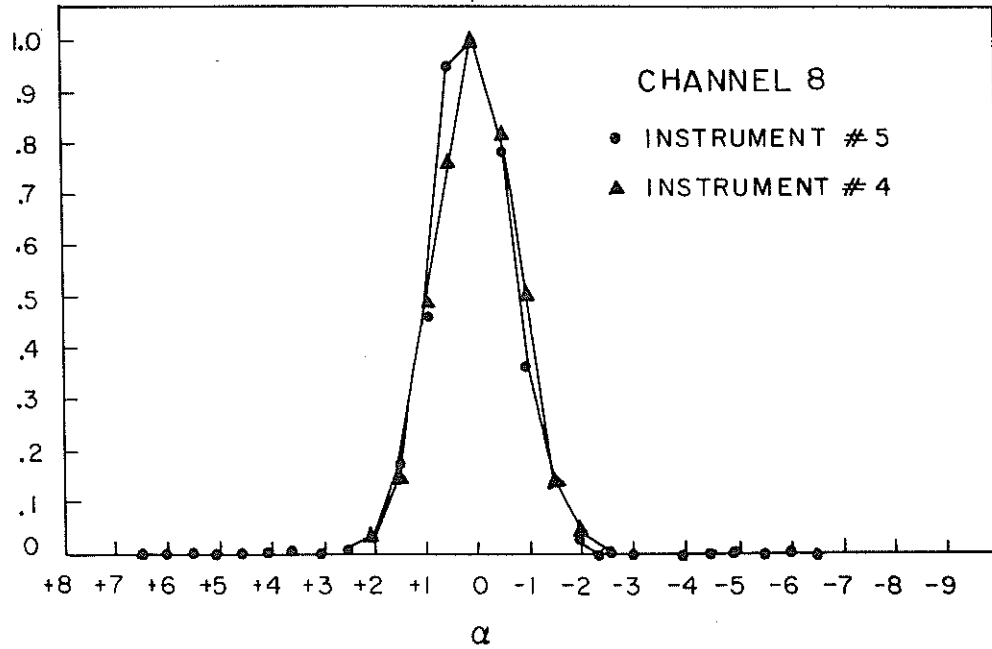
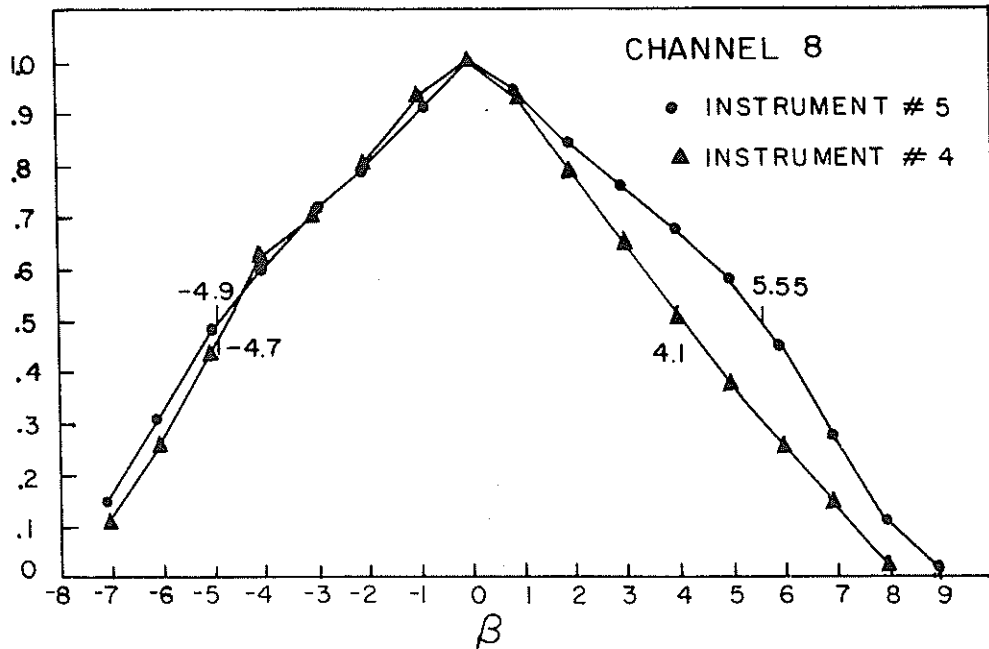


Figure 10. Angular Response of Detectors 4 and 5 on Channel 8. For  $\beta$  the curve is the response along the axis where  $\alpha = 0$  and is normalized to the counts observed when  $\alpha = \beta = 0$ . Similarly for  $\alpha$  the curve is the response along the axis where  $\beta = 0$  and is normalized to the counts observed when  $\alpha = \beta = 0$

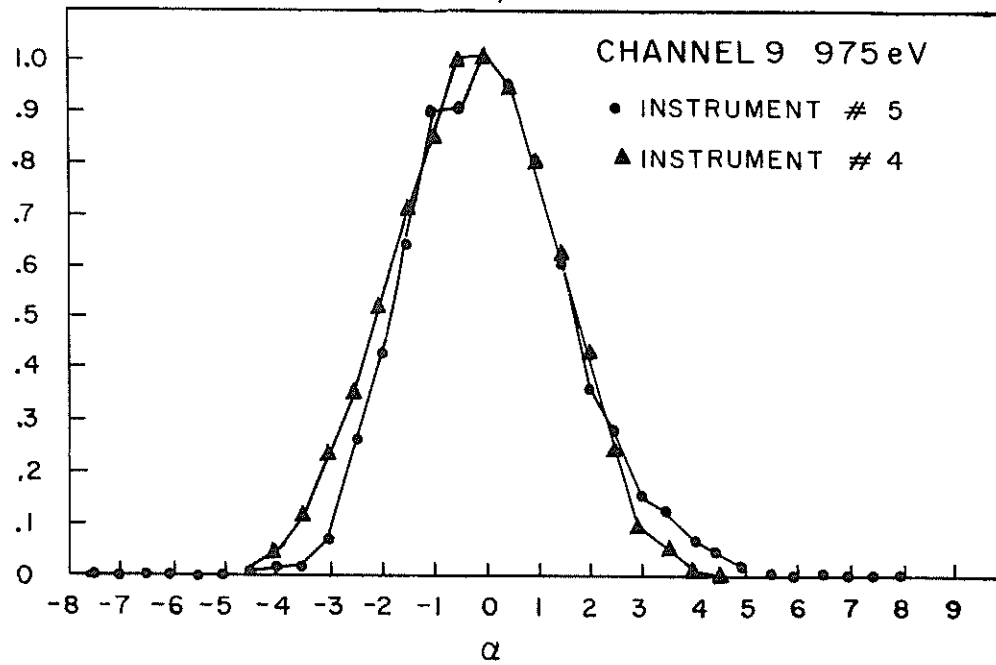
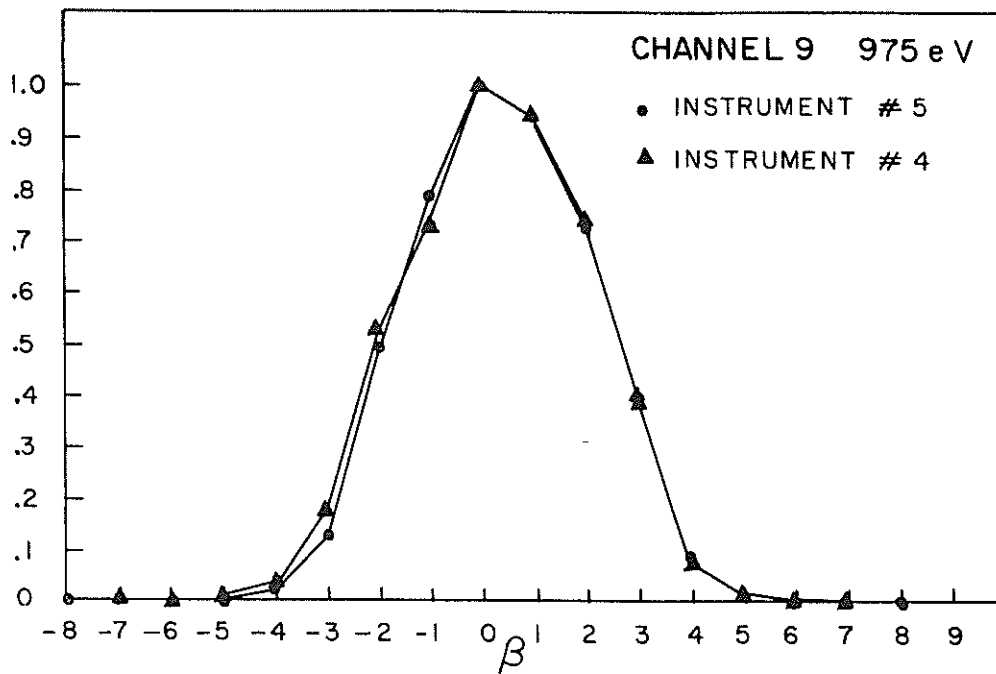


Figure 11. Angular Response of Detectors 4 and 5 on Channel 9. For  $\beta$  the curve is the response along the axis where  $\alpha = 0$  and is normalized to the counts observed when  $\alpha = \beta = 0$ . Similarly for  $\alpha$  the curve is the response along the axis where  $\beta = 0$  and is normalized to the counts observed when  $\alpha = \beta = 0$ .



Table 1. Calibration Figures for Detectors 4 and 5

Channel Instrument	E Peak		$\Delta E$		G Peak		$\int G(E)dE$	
	#4	#5	#4	#5	#4	#5	#4	#5
1	20200 eV	20640 eV	1880 eV	1860 eV	$4.0 \times 10^{-4}$	$4.1 \times 10^{-4}$	$7.98 \times 10^{-1}$	$8.53 \times 10^{-1}$
2	13160 eV	13200 eV	1280 eV	1310 eV	$4.8 \times 10^{-4}$	$5.2 \times 10^{-4}$	$6.35 \times 10^{-1}$	$6.99 \times 10^{-1}$
3	8480 eV	8550 eV	760 eV	785 eV	$6.1 \times 10^{-4}$	$6.4 \times 10^{-4}$	$4.83 \times 10^{-1}$	$5.22 \times 10^{-1}$
4	5500 eV	5550 eV	483 eV	509 eV	$7.2 \times 10^{-4}$	$7.4 \times 10^{-4}$	$3.61 \times 10^{-1}$	$3.88 \times 10^{-1}$
5	3575 eV	3590 eV	322 eV	327 eV	$8.2 \times 10^{-4}$	$8.5 \times 10^{-4}$	$2.71 \times 10^{-1}$	$2.94 \times 10^{-1}$
6	2350 eV	2365 eV	205 eV	216 eV	$9.1 \times 10^{-4}$	$9.4 \times 10^{-4}$	$1.98 \times 10^{-1}$	$2.07 \times 10^{-1}$
7	1525 eV	1550 eV	138 eV	151 eV	$1.0 \times 10^{-3}$	$1.0 \times 10^{-3}$	$1.46 \times 10^{-1}$	$1.54 \times 10^{-1}$
8	997 eV	1003 eV	100 eV	99 eV	$1.06 \times 10^{-3}$	$1.13 \times 10^{-3}$	$1.08 \times 10^{-1}$	$1.10 \times 10^{-1}$
9	972 eV	975 eV	127 eV	103 eV	$3.80 \times 10^{-4}$	$4.50 \times 10^{-4}$	$4.83 \times 10^{-2}$	$4.64 \times 10^{-2}$
10	638 eV	638 eV	84 eV	68 eV	$3.90 \times 10^{-4}$	$4.50 \times 10^{-4}$	$3.28 \times 10^{-2}$	$3.06 \times 10^{-2}$
11	414 eV	410 eV	54 eV	43 eV	$3.80 \times 10^{-4}$	$4.50 \times 10^{-4}$	$2.05 \times 10^{-2}$	$1.94 \times 10^{-2}$
12	267 eV	267 eV	35 eV	28 eV	$3.80 \times 10^{-4}$	$4.50 \times 10^{-4}$	$1.33 \times 10^{-2}$	$1.26 \times 10^{-2}$
13	173 eV	173 eV	23 eV	18 eV	$3.80 \times 10^{-4}$	$4.50 \times 10^{-4}$	$8.74 \times 10^{-3}$	$8.10 \times 10^{-3}$
14	112 eV	113 eV	15 eV	12 eV	$3.80 \times 10^{-4}$	$4.70 \times 10^{-4}$	$5.70 \times 10^{-3}$	$5.60 \times 10^{-3}$
15	73.0 eV	72.2 eV	9.6 eV	9.6 eV	$3.80 \times 10^{-4}$	$4.50 \times 10^{-4}$	$3.65 \times 10^{-3}$	$3.42 \times 10^{-3}$
16	47.0 eV	46.6 eV	6.1 eV	4.9 eV	$2.89 \times 10^{-4}$	$3.40 \times 10^{-4}$	$1.76 \times 10^{-3}$	$1.67 \times 10^{-3}$

Table 2. Channeltron Efficiency

Energy	Efficiency		Archeletor & DeForest	Percent Difference Detector 4	Percent Difference Detector 5
	Detector 4	Detector 5			
20000 eV	0.36	0.39	0.405	-11	-4
13000 eV	0.46	0.45	0.43	7	5
8500 eV	0.57	0.58	0.48	19	21
5500 eV	0.65	0.68	0.56	16	22
3575 eV	0.75	0.77	0.66	14	17
2350 eV	0.83	0.86	0.83	0	4
1550 eV	0.88	0.94	0.94	6	0
1000 eV	1.00	1.00	0.99	0	0

from 2 KeV to 10 KeV the efficiencies derived in this manner are between 10 percent and 20 percent higher than those predicted, while they are in substantial agreement outside this range.

For the four channels 9 to 12 the calibration also yielded consistent results. The peak value for  $G(E)$  in these channels is  $3.8 \times 10^{-4}$  and  $4.5 \times 10^{-4}$  respectively for detectors 4 and 5 and the value of  $\Delta E/E$  is constant as cited previously. The one exception is channel 11 for detector 4. For this case the line shape was maintained but the peak value of  $G(E)$  was  $5.28 \times 10^{-4}$ .

We attribute the anomalously high value to small inhomogeneities in the calibrating beam. As previously mentioned, the beam is produced by illuminating an aluminum plate with a set of UV lamps. The illumination is not perfectly uniform which leads to small inhomogeneities in the beam intensity. As the beam energy is decreased, the radius of curvature for electrons (in whatever residual field that remains within the Helmholtz coils) also decreases, shifting the orientation of the beam slightly. For the calibration of a specific channel, such a shift can place one of these small inhomogeneities at the entrance aperture of one of the detectors. If the beam is more intense in the small region this can lead to an erroneously high value of  $G(E)$  as was observed. We believe this to be the explanation for the results for channel 11 and have assigned it, therefore, the same peak  $G(E)$  as the surrounding channels.

For channels 13 through 16, difficulties were encountered in adjusting the Helmholtz coils to correct for the earth's magnetic field and in maintaining a uniform mono-directional beam. Reasonable numbers were determined for central energy of each channel but the peak value of  $G(E)$  and  $\Delta E/E$  were assumed to be the same as for the four higher energy channels. For channels 13 through 15 the channeltron

efficiency should be unity. For channel 16 the efficiency was calculated from the equation

$$Ee = 0.10E^{0.515} \quad (E \text{ in eV}) \quad (3)$$

from the work of Archuleta and DeForest.<sup>13</sup> All the calibration numbers are listed in Table 1.

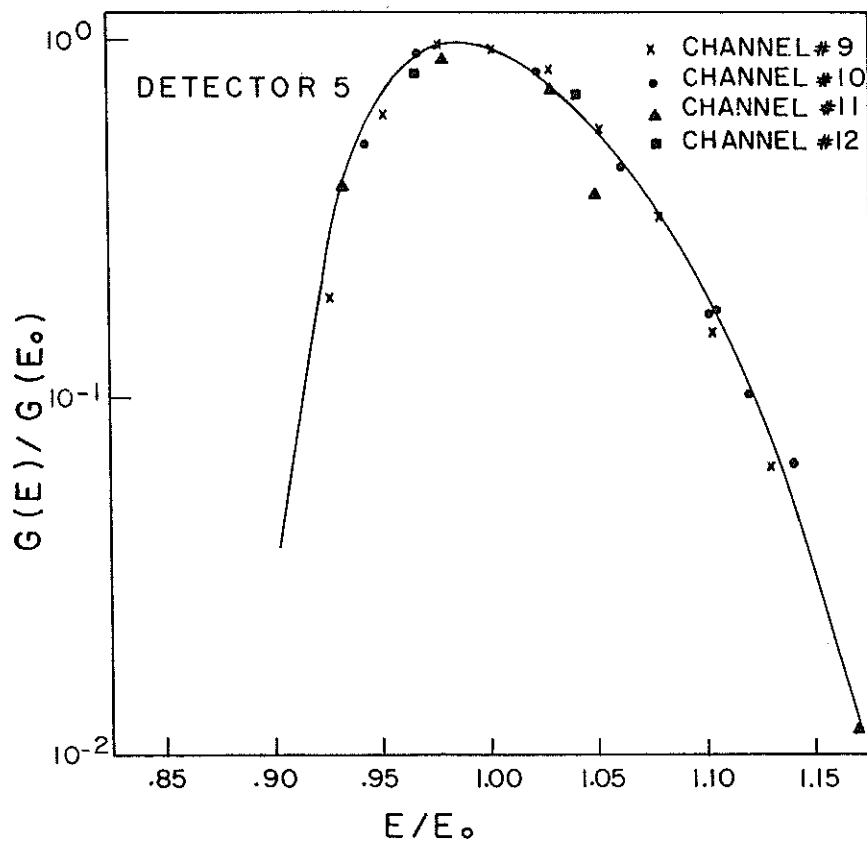


Figure 12. The Energy Dependent Geometric Factor,  $G(E)$ , Normalized to the Peak Geometric Factor,  $G_0(E_0)$ , Plotted as a Function of Energy Normalized to the Channels Central Energy,  $E_0$ . The figure shows the data from channels 9 through 12 for Detector 5

In Figures 12 to 17 the normalized curves for channels 1 to 8 and 9 to 12 for detectors 4 and 5 are shown. The curves were calculated by normalizing the measurements of  $G(E)$  observed in a given channel to the peak value  $G_0(E)$  observed in that channel and by normalizing the energy  $E$ , at which each measurement was made, to the central energy of the channel  $E_0$ . The geometric factors obtained for F2 and F3 by Huber et al.<sup>12</sup> using Monte Carlo techniques are compared to those for F4 and F5 in Table 3. In general the overall agreement is between 10 percent and 20 percent. For channels 1 to 8 the values for the beam calibration are 10 to 20 percent lower than those from the previous calibration. For channels 9 through 16 the beam calibration gives numbers 10 to 20 percent higher than from the work of Huber. We attribute the difference to instrumental uncertainties between the two calibration systems. We believe, however, that the beam calibration at Rice University provides basically more accurate numbers and should be used in future processing.

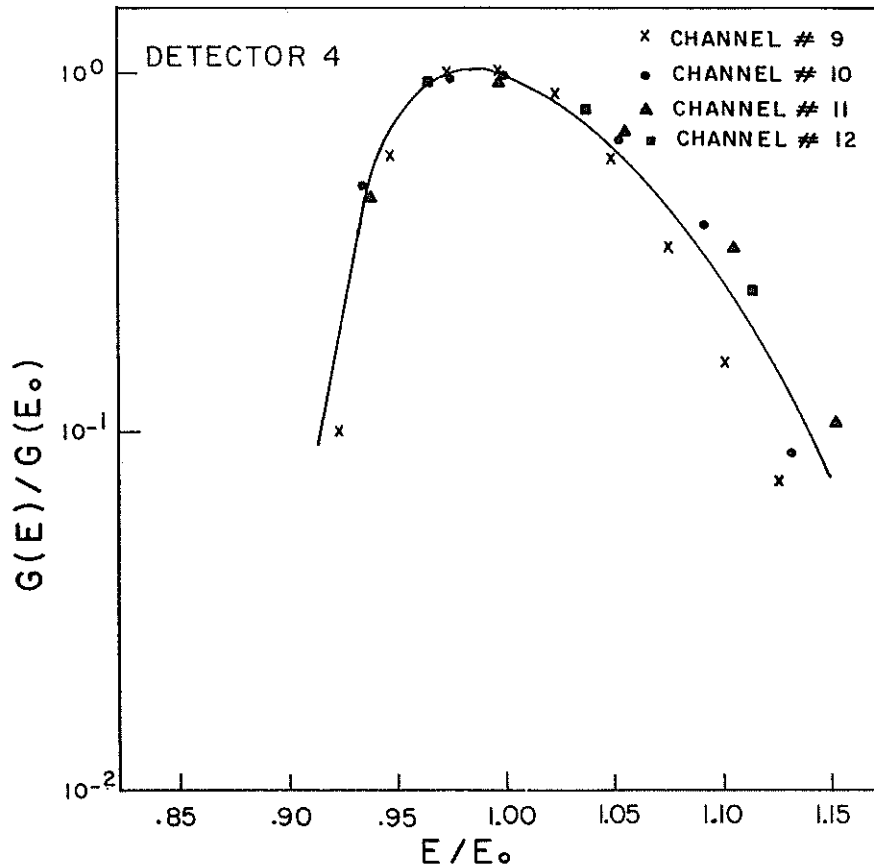


Figure 13. The Energy Dependent Geometric Factor,  $G(E)$ , Normalized to the Peak Geometric Factor,  $G_0(E_0)$ , Plotted as a Function of Energy Normalized to the Channels Central Energy,  $E_0$ . The figure shows the data from channels 9 through 12 for Detector 4

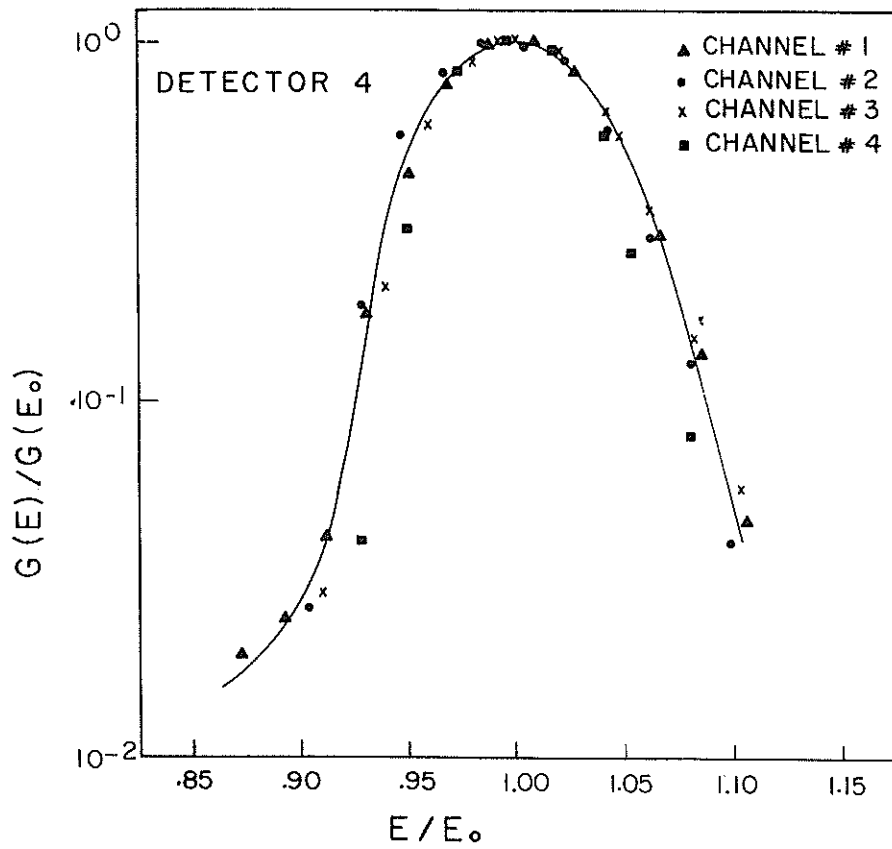


Figure 14. Normalized Curves of the Energy Dependent Geometric Factor as in Figure 12 for Channels 1 Through 4 of Detector 4

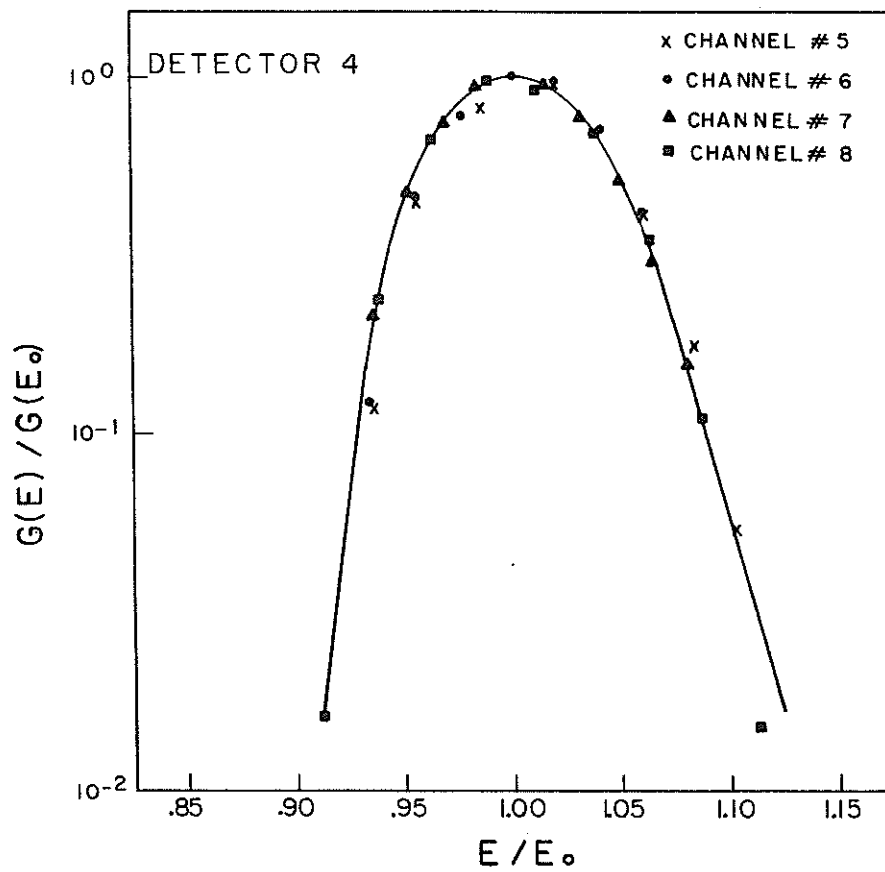


Figure 15. Normalized Curves of the Energy Dependent Geometric Factor as in Figure 12 for Channels 5 Through 8 of Detector 4

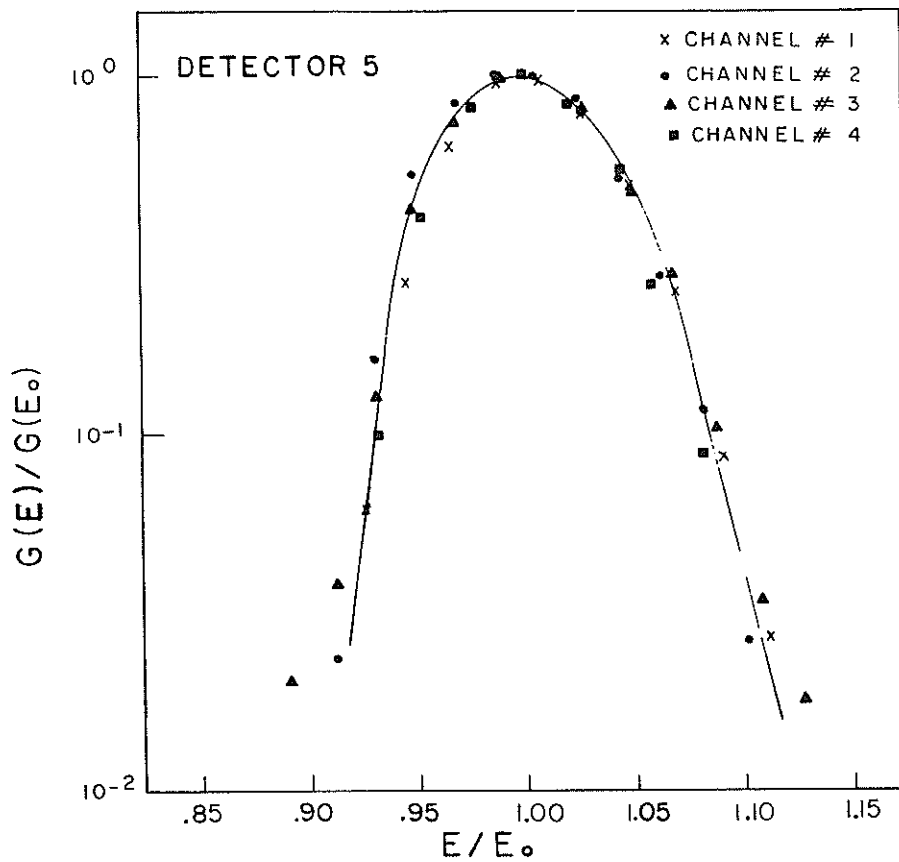


Figure 16. Normalized Curves of the Energy Dependent Geometric Factor as in Figure 12 for Channels 1 Through 4 of Detector 5

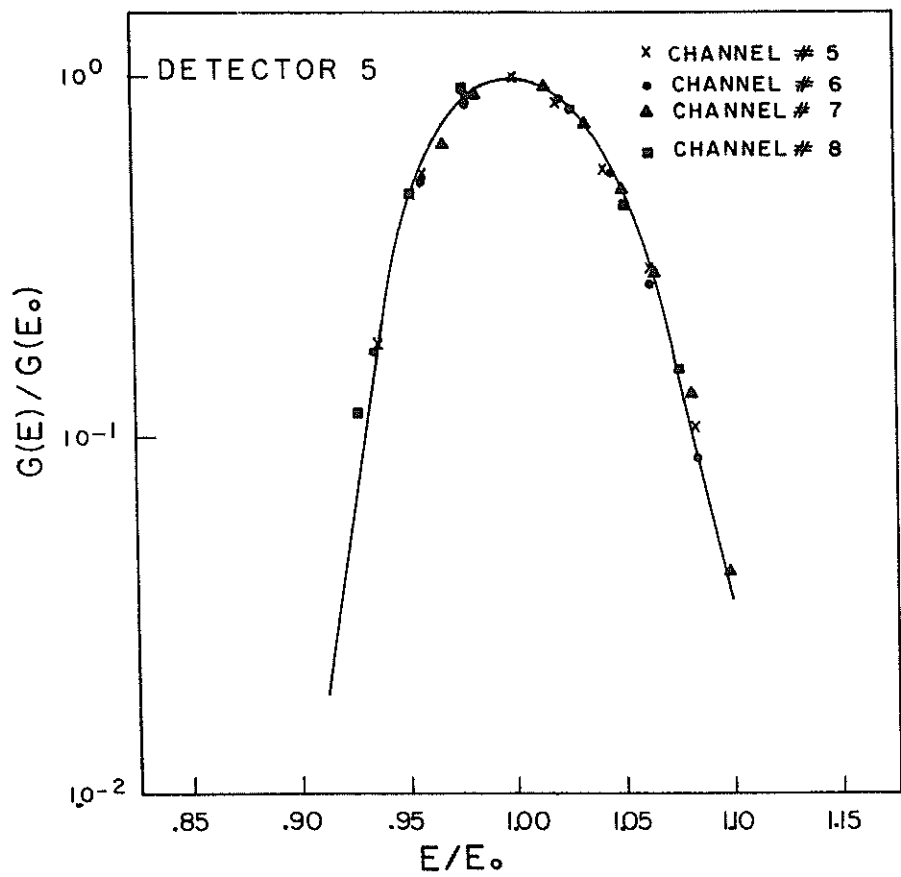


Figure 17. Normalized Curves of the Energy Dependent Geometric Factor as in Figure 12 for Channels 5 Through 8 of Detector 5



Table 3. Comparison of Geometric Factors Derived for Detectors 2 and 3 and Those Derived for Detectors 4 and 5

$$G = \int G(E) dE$$

$$j(E) = \frac{\text{counts}}{\Delta T \cdot G}$$

Channel	#4 F4	#5 F5	#2 and #3 F2
1	$7.98 \times 10^{-1}$	$8.53 \times 10^{-1}$	1.05
2	$6.35 \times 10^{-1}$	$6.99 \times 10^{-1}$	$7.66 \times 10^{-1}$
3	$4.83 \times 10^{-1}$	$5.22 \times 10^{-1}$	$5.59 \times 10^{-1}$
4	$3.61 \times 10^{-1}$	$3.88 \times 10^{-1}$	$4.00 \times 10^{-1}$
5	$2.71 \times 10^{-1}$	$2.94 \times 10^{-1}$	$3.25 \times 10^{-1}$
6	$1.98 \times 10^{-1}$	$2.47 \times 10^{-1}$	$2.47 \times 10^{-1}$
7	$1.46 \times 10^{-1}$	$1.54 \times 10^{-1}$	$1.94 \times 10^{-1}$
8	$1.08 \times 10^{-1}$	$1.10 \times 10^{-1}$	$1.36 \times 10^{-1}$
9	$4.83 \times 10^{-2}$	$4.64 \times 10^{-2}$	$4.49 \times 10^{-2}$
10	$3.28 \times 10^{-2}$	$3.06 \times 10^{-2}$	$2.84 \times 10^{-2}$
11	$2.05 \times 10^{-2}$	$1.94 \times 10^{-2}$	$1.86 \times 10^{-2}$
12	$1.33 \times 10^{-2}$	$1.26 \times 10^{-2}$	$1.13 \times 10^{-2}$
13	$8.74 \times 10^{-3}$	$8.10 \times 10^{-3}$	$7.86 \times 10^{-3}$
14	$5.70 \times 10^{-3}$	$5.60 \times 10^{-3}$	$3.31 \times 10^{-3}$
15	$3.65 \times 10^{-3}$	$3.42 \times 10^{-3}$	$3.31 \times 10^{-3}$
16	$1.76 \times 10^{-3}$	$1.67 \times 10^{-3}$	$1.67 \times 10^{-3}$

#### 4. DATA REDUCTION OF SSJ/3 ON DMSP-F2 AS PERFORMED AT AFGL

The precipitating electron data from DMSP-F2 are displayed as shown in Figure 18. The data is taken from a South Pole pass on July 2, 1978. For each satellite pass the following are plotted as a function of universal time:

- a) The total number flux or integral flux JTOT

$$JTOT = \sum_i j(E_i) \frac{E_{i+1} - E_{i-1}}{2} \quad (4)$$

where  $j(E_i)$  is the differential flux for each energy channel with central energy  $E_i$ . The differential flux is calculated from the count rate by the equation

$$j(E_i) = \frac{C_i/\Delta T}{G(E_i) \Delta E_i} \approx \frac{C_i/\Delta T}{\int G(E) dE} \quad (5)$$

$C_i = \text{particles}$   
 $\Delta T = \text{sec}$   
 $G(E_i) = \text{cm}^2 \text{ster}$   
 $\Delta E_i = \text{eV}$

with  $C_i$ , the counts in the accumulation interval  $\Delta T$ ;  $G(E_i)$ , the energy dependent geometric factor; and  $\Delta E_i$ , the channel width. The total number flux is measured in particles/(cm<sup>2</sup>.ster.sec.);

b) The integral energy flux JETOT

$$\text{JETOT} = \sum_i E_i j(E_i) \frac{(E_{i+1} - E_{i-1})}{2} \quad (6)$$

and is measured in KeV/(cm<sup>2</sup>.ster.sec.);

c) The average energy EAV

$$\text{EAV} = \frac{\text{JETOT}}{\text{JTOT}} \quad (7)$$

The energy is in KeV, and the scale for the average energy is linear.

The universal time is given in seconds with an interval of one minute between tick marks. At two minute intervals ephemeris data is given. The values given are the geographic coordinates of the satellite, the corrected geomagnetic coordinates of the satellite projected along the magnetic field line to 100 km, and the magnetic local time.

The satellite pass in Figure 18 is not to be taken as representative. If anything it is too clean, but as such is useful for discussion of various features of the data. The vertical lines are the best estimates (from changes in the number flux and the energy flux) of the auroral boundaries, both equatorward and poleward. Equatorward of both equatorward boundaries (morning and evening) are regions in which the energy flux and the average energy are inflated. A lesser inflation of the number flux occurs. These increases are produced by high energy particles from the inner radiation belts that penetrate through the detector casing, stimulating the spiraltron directly and giving spurious counts. For moderate and low magnetic activities there is usually a well-defined gap between oval data and inner radiation belt data making it easy to identify and disregard the latter. At higher activities the oval moves equatorward and the two regions can overlap. In these cases care must be taken to differentiate the two populations.

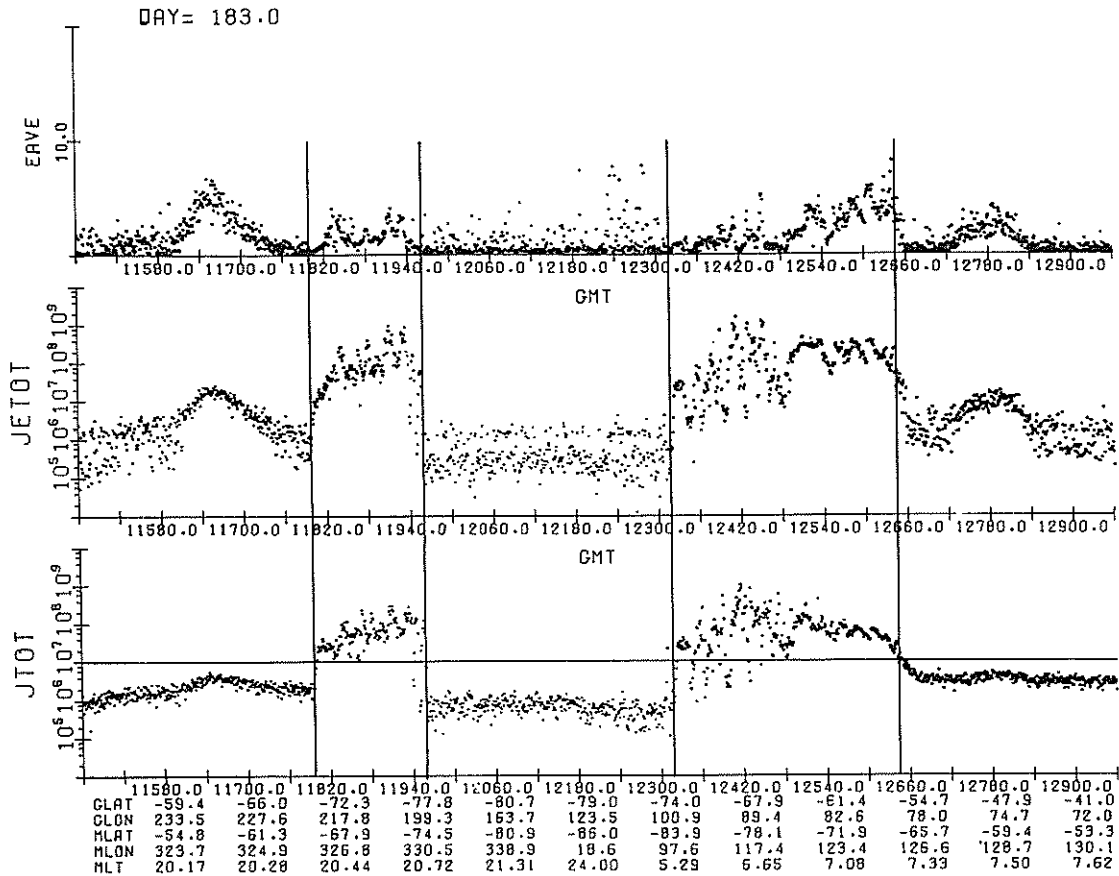


Figure 18. The Format in Which the DMSP-F2 Precipitating Electron Data is Processed. The first panel gives the average energy in keV (the scale is linear); the second panel gives the integral energy flux, JETOT, in keV/cm<sup>2</sup>ster. sec.); the third panel gives the total number flux, JTOT in electrons/(cm<sup>2</sup>ster. sec.). These values are plotted against the following: universal time, geographic coordinates of the satellite, corrected geomagnetic coordinates of the satellite projected along the magnetic field line to 100 km, and the magnetic local time. The data is taken on 2 July 1978. The vertical lines indicate equatorward and poleward oval boundaries, as determined from changes in the number and energy fluxes

For the case shown in Figure 18 the boundaries have the sharpest changes in the energy flux. However, many times a more gradual transition from background in both number and energy fluxes is the case. An example, although not a troublesome one, occurs on the equatorward morning edge in the number flux. Fortunately, the energy flux transition is considerably sharper.

We have found that for cases such as that shown in Figure 18, the oval boundaries we choose from contain sharp changes in the fluxes that correspond closely to the positions where the number flux rises and remains for at least a short period

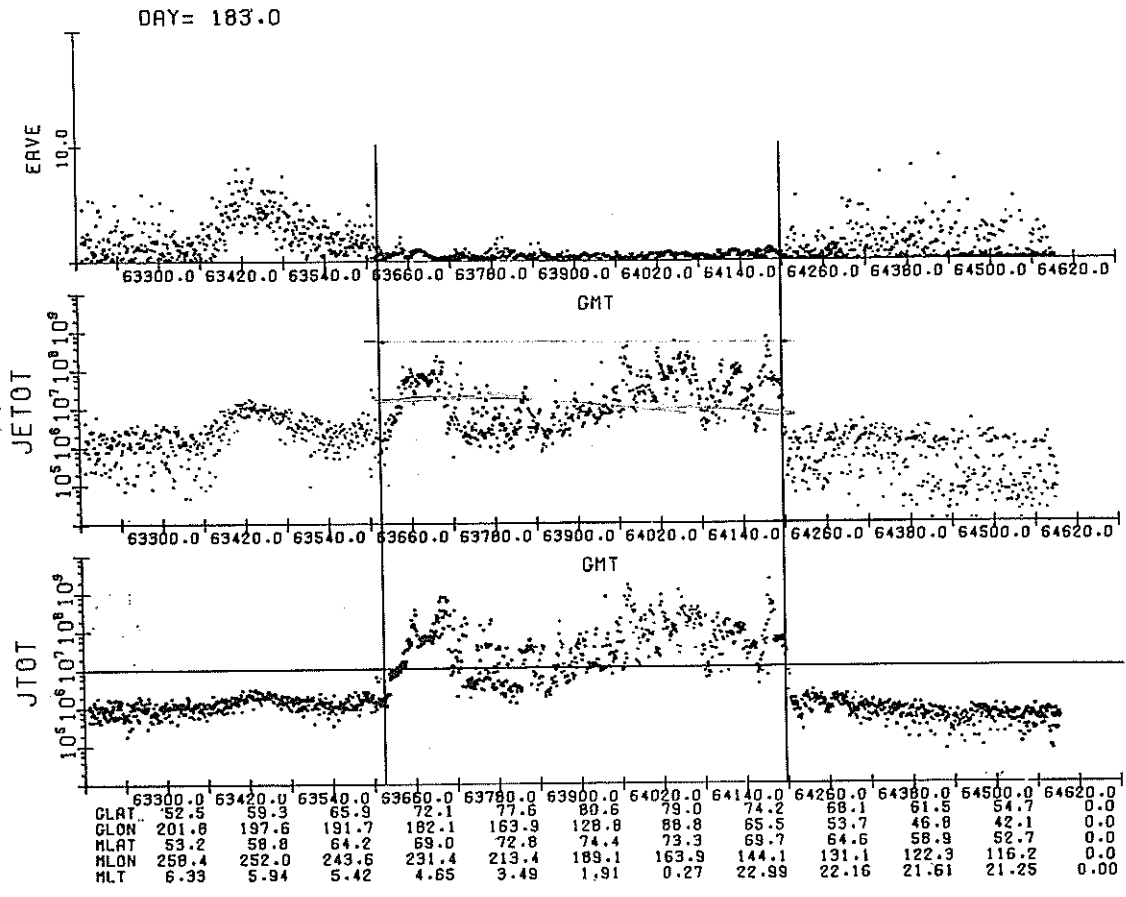


Figure 19. Same as Figure 18, but for a Later UT in Which the Satellite Path does not Enter the North Polar Cap, but Passes Through the Midnight Oval

of time above the  $10^7$  level. In the case shown the boundaries determined by both methods are identical (as shown by the horizontal line at the  $10^7$  level). In Section 5 we will look at the feasibility of using the  $10^7$  level in the number flux as a way of standardizing the definition of auroral boundaries.

As pointed out in Section 2, dawn-to-dusk coverage of the auroral regions and the caps, is obtainable only for DMSP-F2 in the first 11 hours of UT. After this time the North Pole subsatellite track lies below  $80^\circ$ , often remaining in the midnight sector throughout. Figure 19 shows a North Pole pass later on July 2, 1978. The equatorward boundaries are clear and are marked. Poleward, however, there is continuity in all quantities from morning to evening making it unclear where the satellite enters the polar cap, if at all. Figure 20 shows a South Pole pass at approximately 13:30 UT. The subsatellite track passes through the midday region

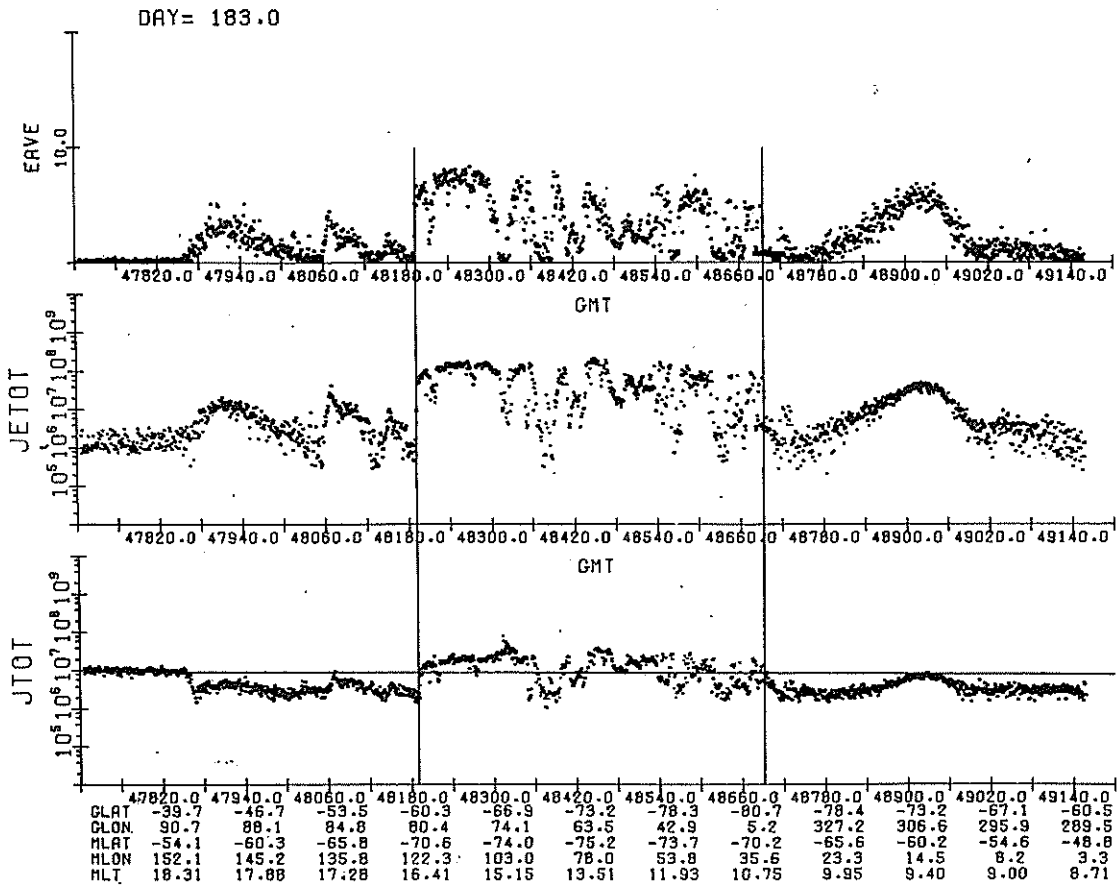


Figure 20. Same as Figure 18, but for a later UT in Which the Satellite Path does not Enter the South Polar Cap, but Passes Through the Midday Oval, or the Cusp Region

near the cusp, and again, never clearly enters the polar cap. The equatorward boundaries, as determined by the criterion  $JTOT > 10^7$ , are designated. There is some structure equatorward of these boundaries, particularly on the evening side that is not associated with spurious counts from inner radiation belt particles. The South Pole pass, one pass later, is shown in Figure 21. Here the subsatellite track passing below the cusp misses the oval entirely.

In Figures 22 to 24 we demonstrate the total information capacity of DMSP-F2 in dealing with the auroral regions. Figure 22 shows the DMSP image from January 3, 1978 at around 15 UT gridded in corrected geomagnetic coordinates. Figure 23 is the corresponding precipitating electron data in the form already discussed. Figure 24 shows ten differential energy spectra for ten successive

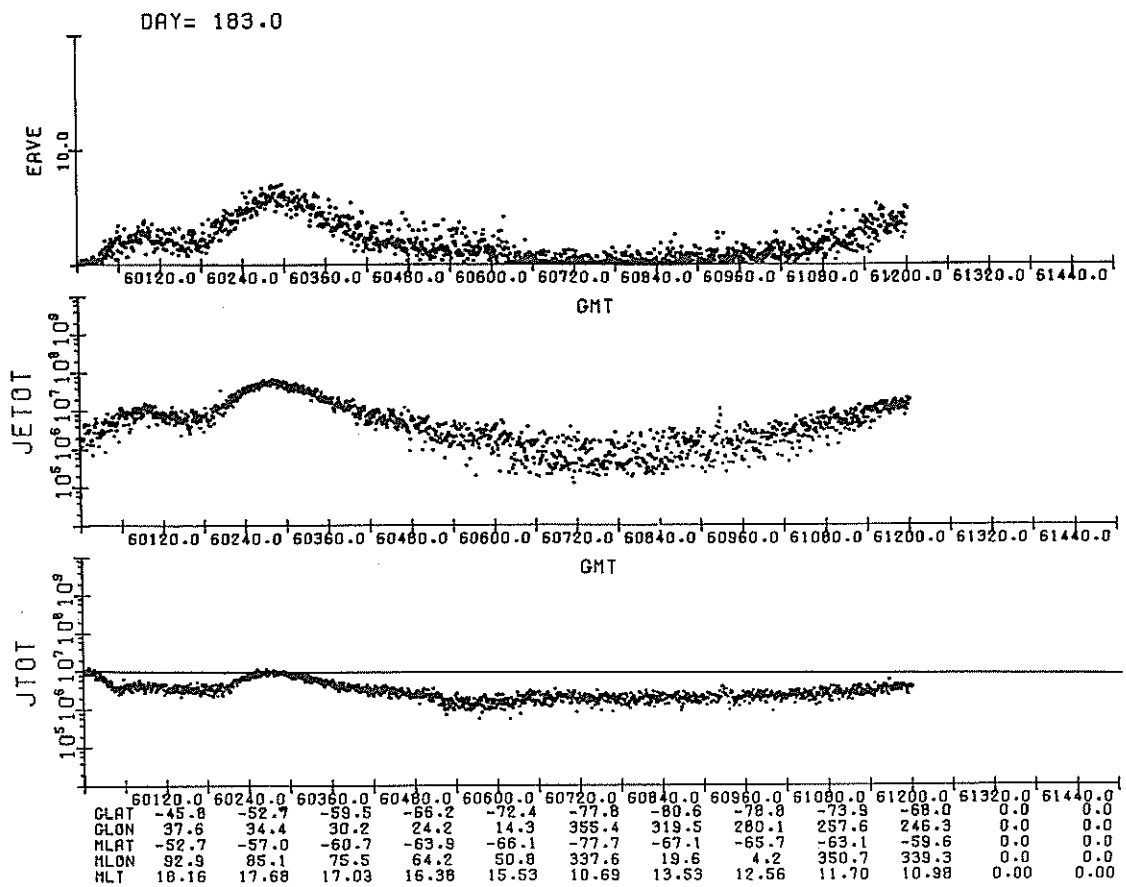


Figure 21. Same as Figure 20, but for a Later UT in Which the Satellite Path is Always Equatorward of the Midday Oval

seconds showing the transition from the most equatorward discrete arc in the evening to the evening diffuse aurora. A display of spectra such as this is available for any ten second interval throughout the high latitude pass.

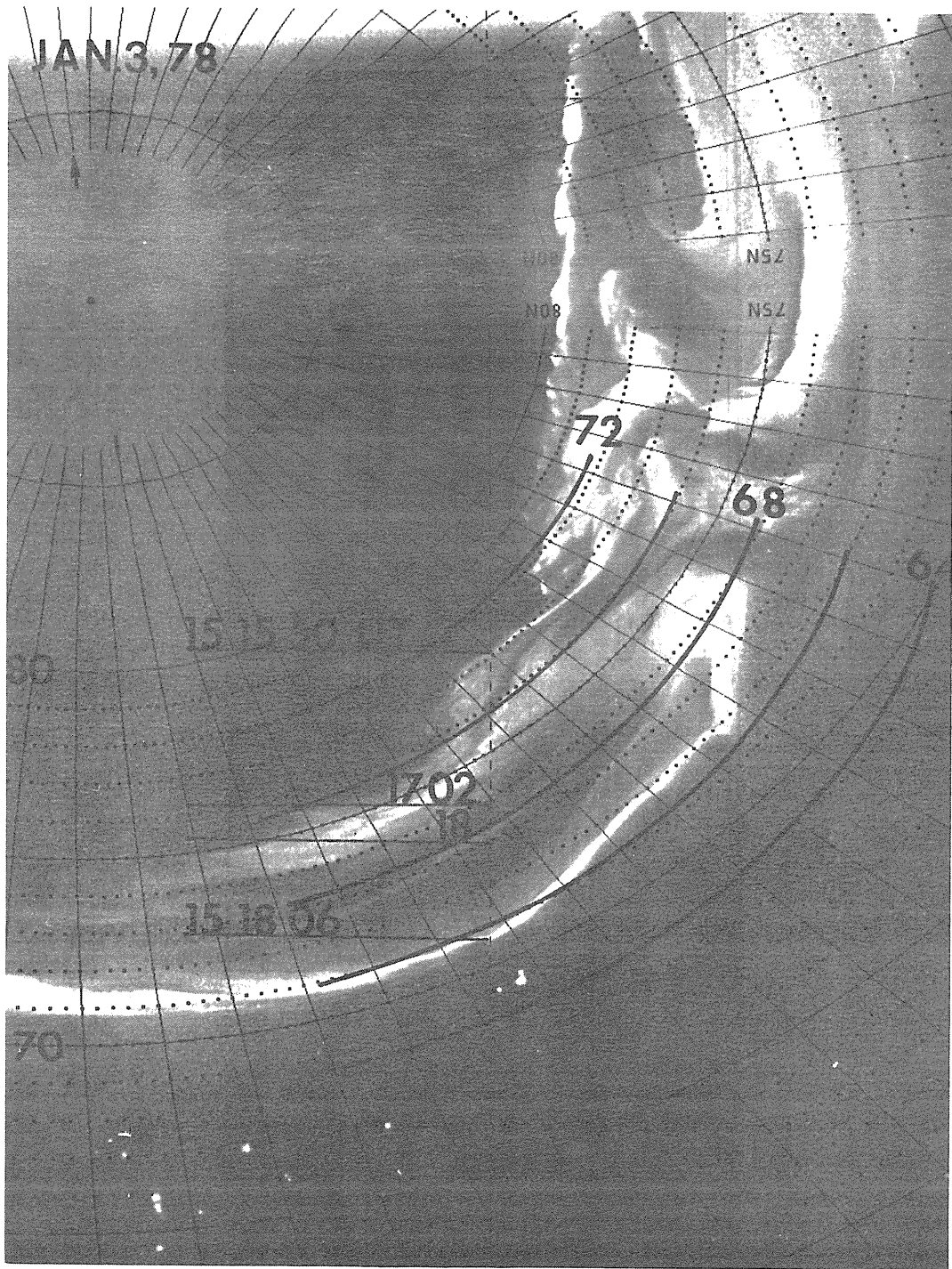


Figure 22. The DMSP-F2 Image for 3 January 1978, Near 15 UT Gridded in Corrected Geomagnetic Coordinates

$1.6 \times 10^{-9}$   
 $6.25 \times 10^8$

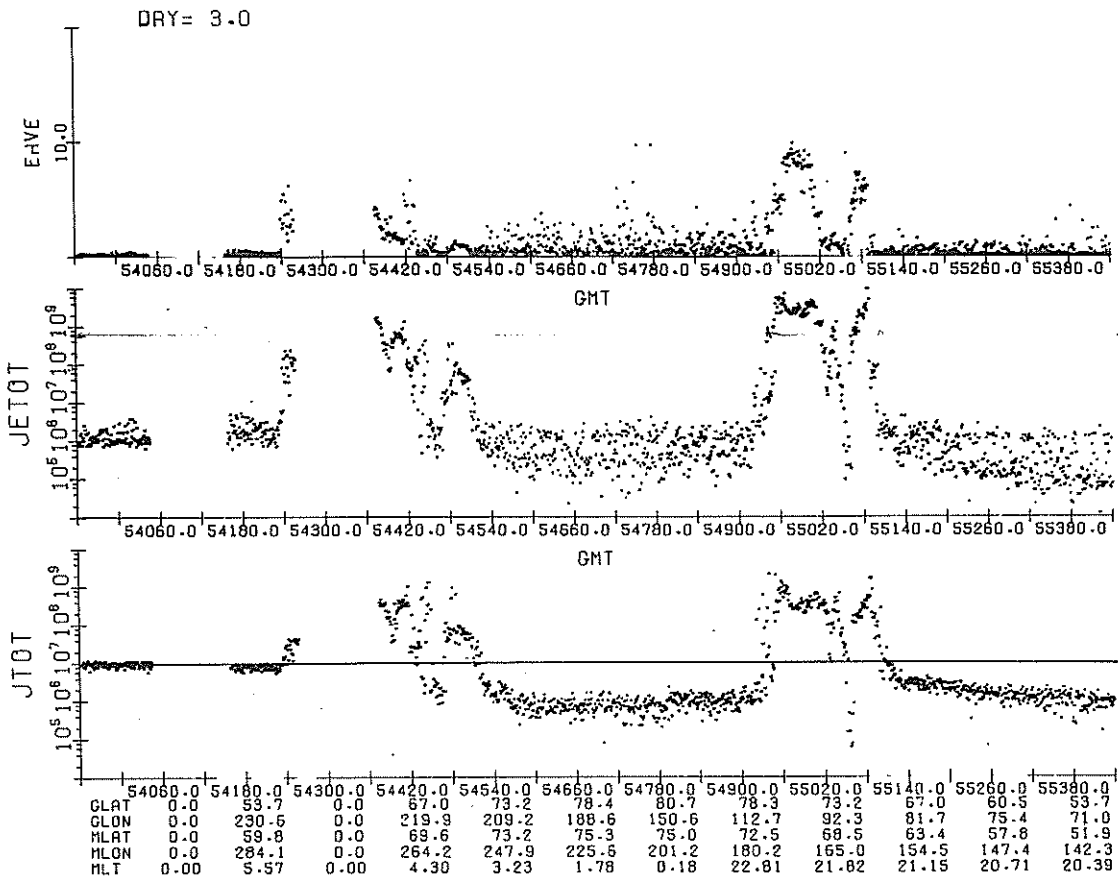


Figure 23. The Precipitating Electron Data for the DMSP-F2 Pass on 3 January 1978, Near 15 UT (Whose Auroral Image is Shown in Figure 22). The format is the same as that for Figure 18



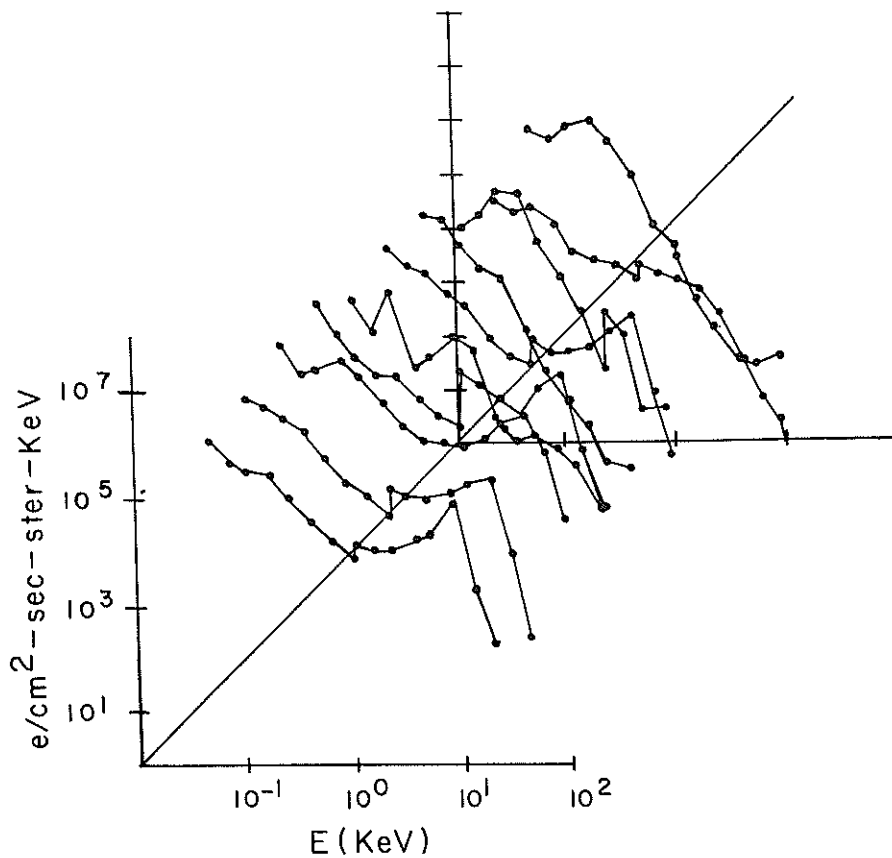


Figure 24. Ten Differential Energy Spectra for Ten Successive Seconds of DMSP-F2 Precipitating Electron Data Taken on 3 January 1978 at 15-18-5 to 15-18-14 UT

## 5. EXAMINATION OF DATA FROM FOUR PASSES

In the following the precipitating electron data for four passes (successive north-south pole passes during an active time and successive north-south pole passes during a quiet time) are examined. We are particularly interested in determining oval (and, therefore, cap) boundaries in a consistent way from the data. From an examination of two months of data it appeared that choosing the position where the total number flux first rose and then fell from  $10^7$  particles/ster.cm<sup>2</sup>.sec. was a good definition of the equatorward and polar boundaries. Therefore, the primary focus of the discussion of the four passes will be boundary determination and the problems involved in this process. Other points of interest will be mentioned as well.

The precipitating electron data are given in Figures 25 to 28.

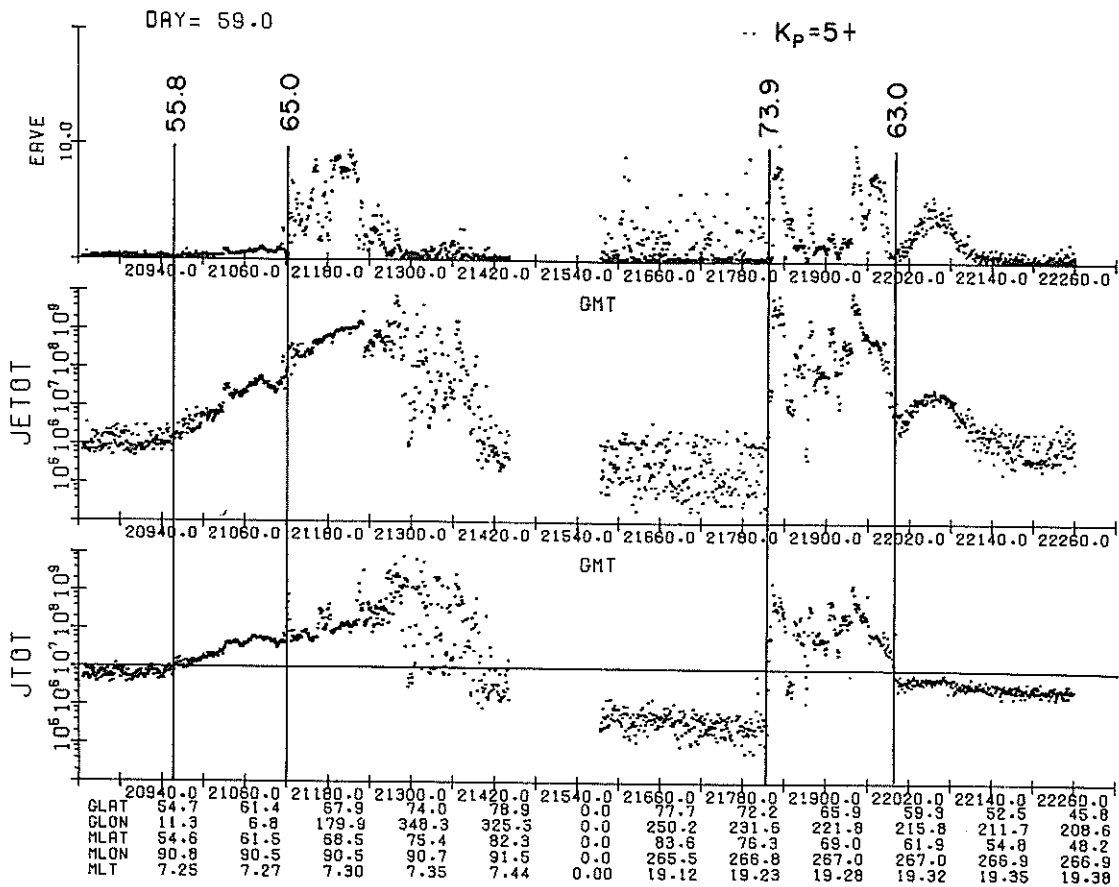


Figure 25. DMSF-F2 Precipitating Electron Data for a North Polar Pass During High Magnetic Activity. Equatorward and poleward oval boundaries are marked by vertical lines. See text for a discussion of the methods used for boundary determination

### 5.1 North Pole Active: 28 February 1978; K<sub>p</sub> = 5+ (Figure 25)

#### 5.1.1 EVENING EQUATORWARD

The equatorward boundary is placed at 63.0° (magnetic latitude).

The JTOT = 10<sup>7</sup> boundary is identical to the best choice of where JTOT rises out of background. The rise is fairly steep.

For JETOT and EAV the expanded oval values begin to overlap the spurious counts from the inner radiation belt, obscuring the equatorward boundary.

EAV rises from background levels approximately 1° higher than the equatorward boundary, or at 64°. This is also the approximate place where JETOT > 10<sup>8</sup>; a minimum value for auroral forms to be seen in DMSF images. The rise in average energy above 64° is very steep.

### 5.1.2 EVENING POLEWARD

The poleward boundary is placed at  $73.9^\circ$ .

Again the  $JTOT = 10^7$  boundary and the best choice of all parameters falling back to background levels are identical. In this case, the last visible arc on DMSP (where  $JE\ TOT > 10^8$ ) and the poleward boundary are nearly coincident.

### 5.1.3 MORNING EQUATORWARD

The morning equatorward boundary using the  $JTOT = 10^7$  criterion is  $55.8^\circ$ . This is also the position for the  $JTOT$  and  $JETOT$  rise from background. However, the rise is very slow and, even though the rise is associated with a rise in average energy, this boundary is nearly  $10^\circ$  lower than the boundary at which  $JETOT$  is above the threshold for visible auroras. ( $JETOT > 10^8$  occurs at  $65^\circ$ .) That the slow rise might be due to spurious counts due to penetrating particles is rejected since the modulation in the average energy is not characteristic of that for spurious counts. Since the selection of the boundary is so dependent on the criterion used, some ambiguity remains for cases such as these.

### 5.1.4 MORNING POLEWARD

The morning poleward boundary cannot be accurately determined because of the data gap (caused by the transmission of data to ground). It appears, however, that the gap lies just poleward of the position where  $JETOT$  and  $JTOT$  fall to background.

Characteristic of morning poleward electron fluxes is high variability in  $JTOT$  and  $JETOT$ , while the equatorward values are more uniformly increasing, suggestive of two distinct types of electron population that are contiguous. If two such populations also exist on the evening side they would have to be superposed to a much greater extent than in the morning to give the observing variations in the fluxes there. The variable morning population has, in this case, considerably lower average energy than the more uniform equatorward population.

Typically the peak average energy in the morning is greater than that in the evening although for this case the difference is not great.

## 5.2 South Pole Active: 28 February 1978; $K_p = 4+$ (Figure 26)

This is the pass following the North Pole pass discussed above.

### 5.2.1 EVENING EQUATORWARD

The equatorward boundary is placed at  $-61.9^\circ$  using the criterion that  $JTOT > 10^7$ . This choice gives a value somewhat higher than the position of  $JTOT$  rising out of background. However, it appears from the average energy values equatorward of this boundary that the small rise in number flux may be caused by

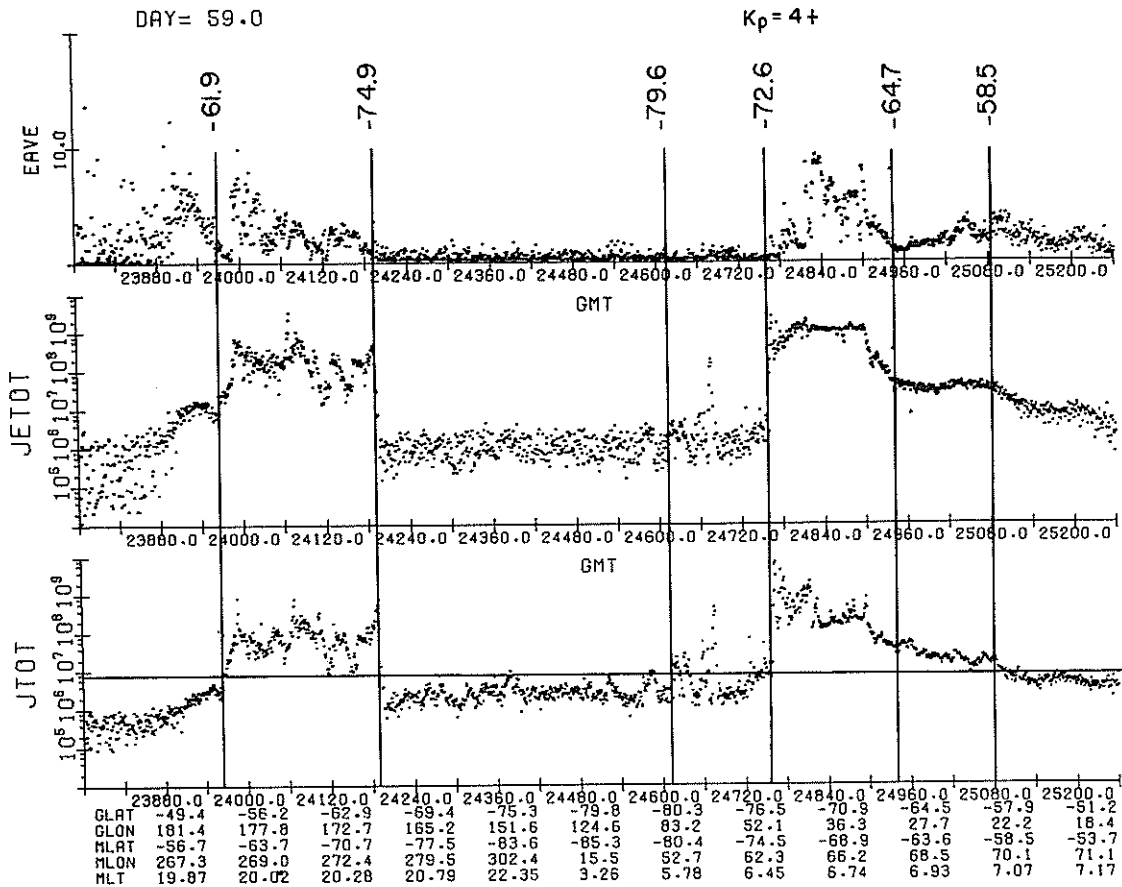


Figure 26. DMSF-F2 Precipitating Electron Data for a South Polar Pass During High Magnetic Activity. Equatorward and poleward oval boundaries are marked by vertical lines. See text for a discussion of the methods used for boundary determination

the spurious counts. In any case the  $10^7$  method places the boundary at the sharpest change in number and energy fluxes and is near the position at which  $JETOT \sim 10^8$  (on the position of near-visible aurora). As in the north pole active case, the strong rise in average energy occurs considerably poleward of this boundary.

### 5.2.2 EVENING POLEWARD

The evening poleward boundary is placed at  $-74.9^\circ$ . Sharp discontinuities in all quantities as well as the  $JTOT = 10^7$  position occur at this value.

There are variations in the number flux across the cap which rise briefly to values as much as  $10^7$ ; if they were stronger, these variations could cause ambiguity in determining a poleward boundary.

### 5.2.3 MORNING EQUATORWARD

As in the North Pole active case the morning equatorward boundary presents two choices, quite different and made more problematic by the spurious counts which occur in the region where the number flux is rising out of background. The  $J_{TOT} = 10^7$  boundary is at  $-58.5^\circ$  and is suspect because of the spurious data. Discontinuities in the energy flux and the average energy occur at  $-64.7$  and probably provide the more reliable estimate.

### 5.2.4 MORNING POLEWARD

The morning poleward boundary is placed at  $-72.6$ . The South Pole boundary is clearer than the corresponding North Pole boundary, the background fluxes being less continuous into the cap than seen in Figure 25. Fluxes greater than  $10^7$  do arise, however, out of the background at higher latitudes. If we required all fluctuations in the number flux to remain below the  $10^7$  level, the morning poleward boundary would be placed at  $-79.6^\circ$ .

## 5.3 Some Comments on the Active Cases

The polar caps are quite evident in the two active cases discussed here. The polar cap fluxes in the North Pole show a smooth variations from  $\sim 4 \cdot 10^6$  particles/ster  $\text{cm}^2$  sec in the morning to  $\sim 4 \cdot 10^5$  particles/ster  $\text{cm}^2$  sec in the evening. In the South Pole the fluxes vary in the opposite sense, a phenomenon discussed by Meng et al<sup>5</sup> and related by him to the y-component of the interplanetary magnetic field. According to Meng, the flux gradient shown here would indicate a positive y-component in the IMF. The provisional indices for February 1978 show an away sector at this time (Lincoln<sup>14</sup>) which normally occur with positive  $B_y$ . The South Pole fluxes are more variable than those in the North Pole but range from  $10^6 - 10^7$  particles/ster  $\text{cm}^2$  sec, more than double the North Pole range.

The equatorward background levels in the South Pole are lower than in the North Pole, as would be expected if the electron population producing this background level is primarily photoelectrons in this region. The South Pole is in daylight and produces more photoelectrons than the North Pole. These low energy electrons travel up the field line and precipitate in the conjugate hemisphere and are detected by the J-sensors.

The evening boundaries are much sharper than the morning boundaries, there being strong discontinuities in the fluxes there. The general trend of the total fluxes in the morning oval is much more continuous for both boundaries and more slowly varying.

14. Lincoln, J. Virginia (1978) Geomagnetic and solar data, J. Geophys. Res. 83:232, 744.

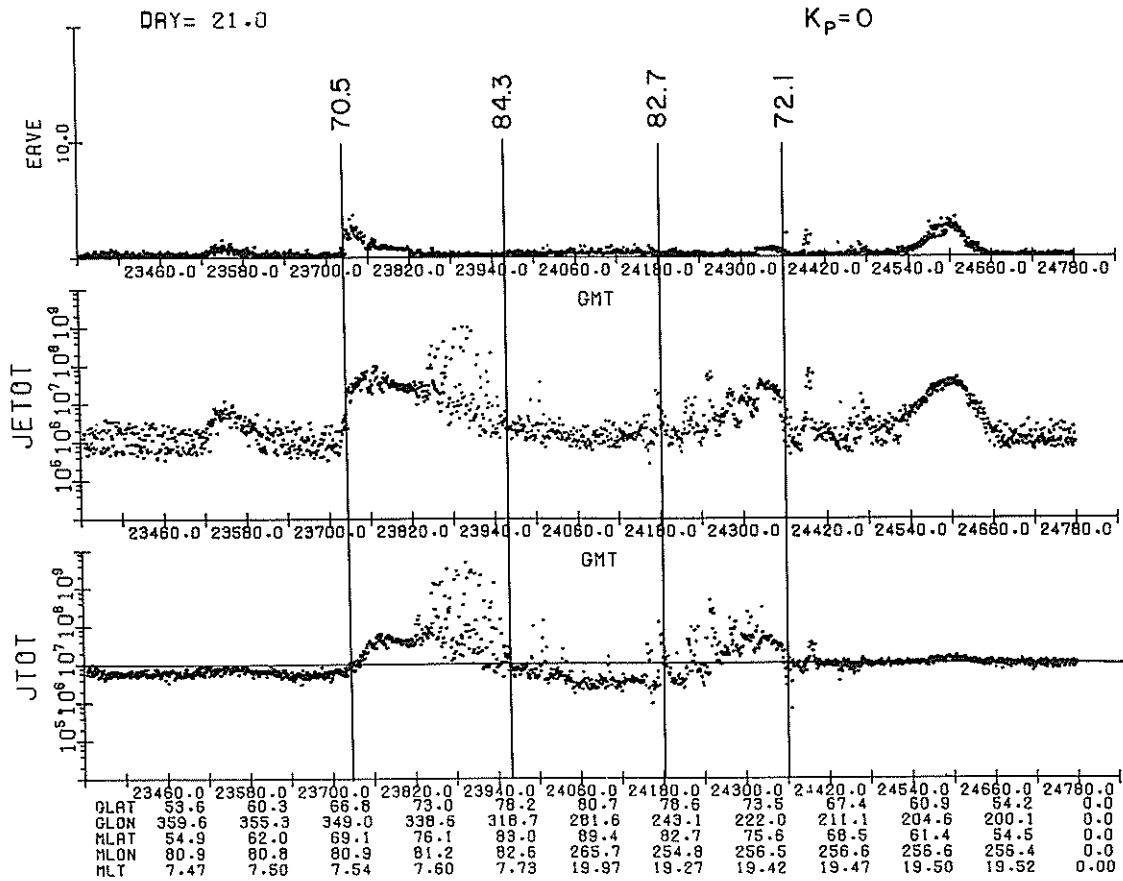


Figure 27. DMSF-F2 Precipitating Electron Data for a North Polar Pass during Low Magnetic Activity. Equatorward and poleward oval boundaries are marked by vertical lines. See text for a discussion of the methods used for boundary determination

#### 5.4 North Pole Quiet: 21 January 1978, Kp = 0 (Figure 27)

The boundaries determined by the  $10^7$  limit in particle flux background levels (ignoring polar scatter and the equatorward spur on the evening side) are:

	<u>Equatorward</u>	<u>Poleward</u>
Morning	70.5°	84.3°
Evening	72.1°	82.7°

It is apparent, however, that the assignment of poleward boundaries has very little meaning: the variations in both the number and the energy flux are completely continuous (that is, bowl-shaped) across the cap. The morning poleward signature

discussed for the active cases (that is, considerable variability in fluxes poleward of smooth fluxes) is present here, both on the morning and evening sides of the oval. There is a small spur of high energy particles equatorward of the  $10^7$  boundary on the evening side. It is clear that whatever leads to a sharp differentiation between the cap and oval in active times is absent for the quiet time shown here. If asymmetric convection is the cause of particle gradients in the cap as suggested by Meng et al<sup>5</sup> they may be considerably lessened or less asymmetric in quiet times. (Provisional data of Lincoln<sup>14</sup> show the IMF to be in an away sector here as well.)

The average energies are considerably reduced for quiet times. The peak average energy in the morning is greater than that in the evening.

The minimum number flux in the cap is  $\sim 4 \cdot 10^6$  particle/ster  $\text{cm}^2 \text{sec}$ .

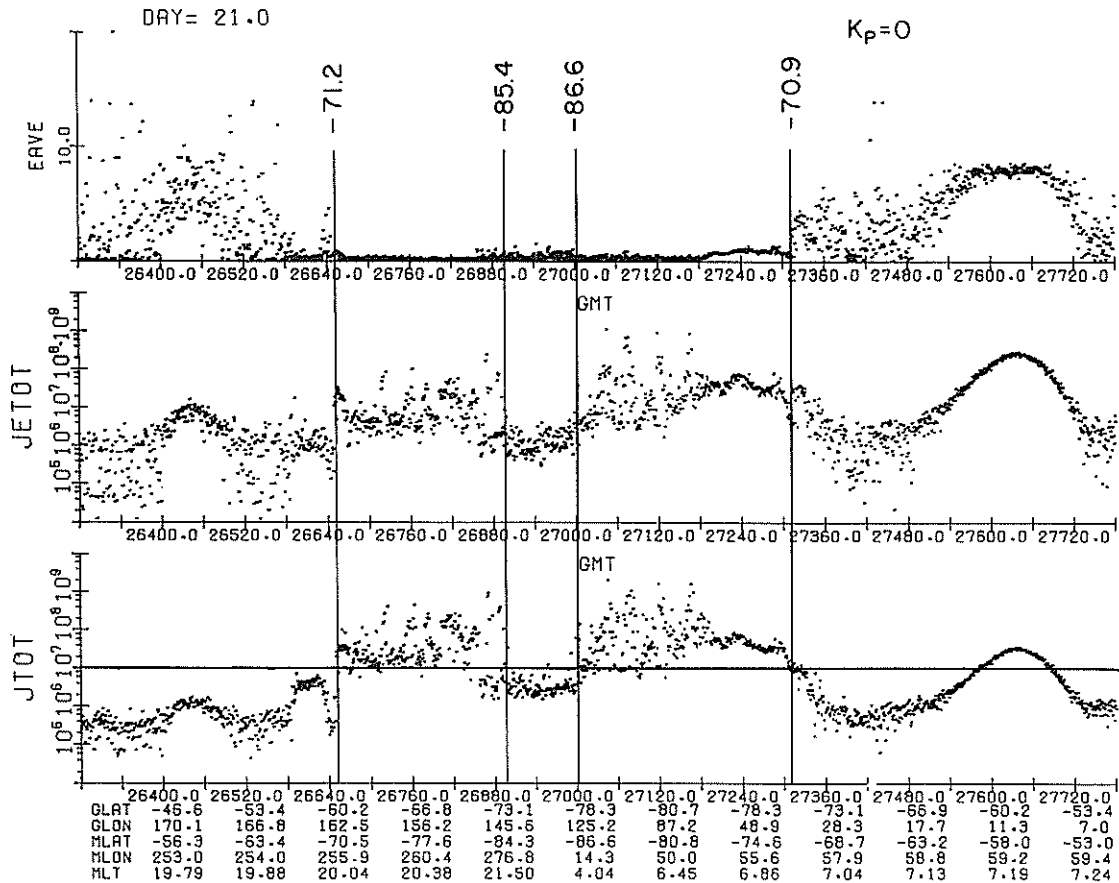


Figure 28. DMSP-F2 Precipitating Electron Data for a South Polar Pass During Low Magnetic Activity. Equatorward and poleward oval boundaries are marked by vertical lines. See text for a discussion of the methods used for boundary determination

### 5.5 South Pole Quiet: 21 January 1978, Kp = 0 (Figure 28)

The south polar cap is more clearly defined than the north polar cap, being a region of comparatively low, uniform flux. The flux in the cap, however, is higher than that in the North Pole, reaching values of  $10^7$  particles/ster  $\text{cm}^2$  sec. If slightly higher, such fluxes would preclude use of the  $10^7$ /level. Nevertheless, we continue to use it here. The  $10^7$  boundaries are

	<u>Equatorward</u>	<u>Poleward</u>
Morning	-70.9°	-86.6°
Evening	-71.2°	-85.4°

There is an interesting spur-like feature below the evening equatorward boundary which remains for several passes, exceeding the  $10^7$  level in JTOT. In this case, the spur is not a problem and such problems can generally be avoided if we require flux levels to reach and stay at or about  $10^7$ . The evening oval for this very quiet time has almost no modulation in the average energy.

## 6. CONCLUSION

For both quiet time cases the total energy flux is below the needed threshold to produce arcs detectable by DMSF. Despite this fact, the electron precipitation reveals a fairly well-defined oval and cap structure (at least as well-defined as for active times), although the problems of definition are somewhat different.

In Figure 29 the oval boundaries for the four cases are compared. The heavy lines are the boundaries determined by the  $10^7$  criterion. The dashed lines indicate other determinations of the boundaries as discussed in the text. The shaded area denotes the variation in boundary definition. Two points stand out:

- a) The boundaries are highly variable.
- b) There are fewer discrepancies (none here) in determining both evening boundaries. Both poleward and equatorward boundaries in the morning side are difficult to consistently determine independent of magnetic activity.

In addition to the problems in determining auroral boundaries, we find the cases discussed here representative of much of the surveyed data in the following ways:

- a) The morning oval is wider than the evening oval.
- b) The number and energy fluxes in the morning oval seem to be composed of two contiguous parts; a smoothly varying equatorward region with small fluctuations, and a highly varying poleward part. The morning oval always has this composition. At times, the evening oval can have a similar composition,



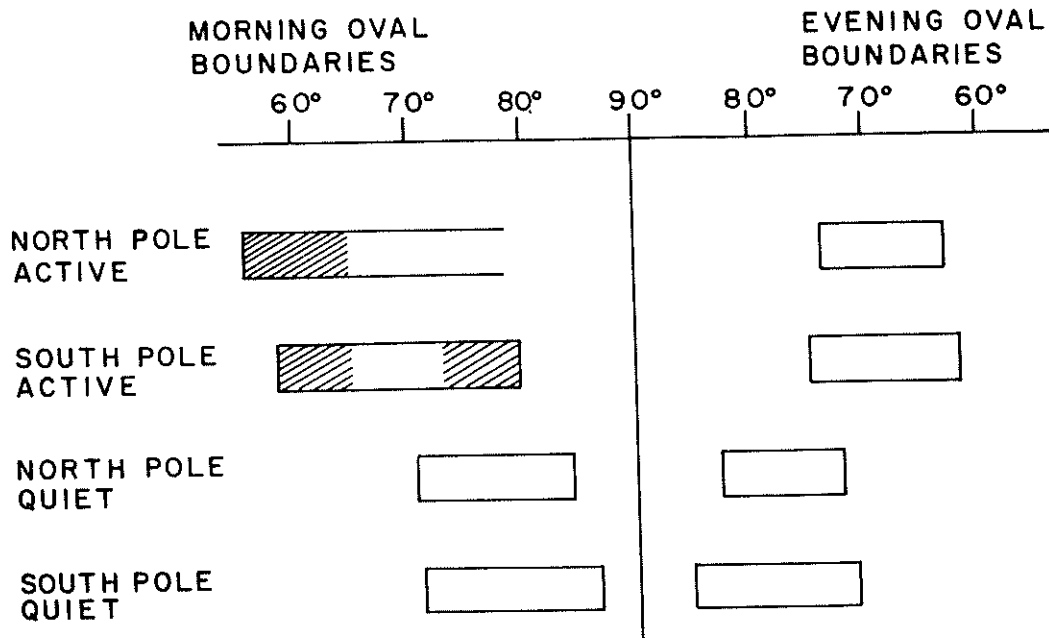


Figure 29. Summary of the Oval Size for Active and Quiet Magnetic Conditions as Determined from the Poleward and Equatorward Boundaries in Figures 25 to 28. Cross-hatched areas denote the range over which the boundary is indeterminate

but it more typically appears to be similar to the equatorward region in the morning with somewhat greater fluctuations and sharper boundaries. An alternative description is a single region that would result if the two morning regions were superimposed.

c) The polar cap fluxes here are remarkably smooth and low between  $2 \cdot 10^5$  and  $2 \cdot 10^6$  particles/ster  $\text{cm}^2$  sec. The low number count rates are reflected in the large statistical scatter in the average energy.

d) The average energy has more gradual transitions inside the oval than the fluxes.

e) The peak average energy is generally higher in the morning than the evening.

f) The equatorward oval boundaries are reasonably symmetrical dawn to dusk.

g) The poleward oval boundaries are highly asymmetric as a result of the larger morning oval. The morning poleward boundary often reaches values  $>80^\circ$  magnetic latitude.

From this lengthly analysis of four passes, several questions suggest themselves regarding the use of this data to monitor real time magnetospheric and solar wind conditions.

1. If we wish to have a real time indicator of auroral activity by making use of equatorward boundaries in electron particle precipitation should that determination be confined to the more well-behaved evening sector?

2. Is there a better indicator of auroral activity than oval boundaries (for example, the peak in the average energy)?

3. Can the difference in polar fluxes be used to determine IMF sectors? If so, can it be made quantitative as well?

4. Is there a near constant particle flux into the polar regions irrespective of magnetic activity? The evening oval size as shown in Figure 29 remains remarkably the same for the wide span in activity, and the number fluxes for active and quiet times are quite comparable. (Compare Figures 25 to 28.) Does this indicate a steady source of electrons with major variations between quiet and active times caused by variations in acceleration mechanisms?

## References

1. Mizera, P.F., Croley, Jr., D.R., Morse, F.A., and Vampola, A.L. (1975) Electron fluxes and correlations with quiet time auroral arcs, J. Geophys. Res. 80:2129.
2. Mende, S.B. and Eather, R.H. (1976) Monochromatic all-sky observations and auroral precipitation patterns, J. Geophys. Res. 81:3771.
3. Eather, R.H. (1979) DMSP Calibration, J. Geophys. Res. 84:4134.
4. Smiddy, M., Sagalyn, R.C., Sullivan, W.P., Wildman, P.J.L., Anderson, P., and Rich, F. (1978) The Topside Ionosphere Plasma Monitor (SSIE) for the Block 5D/Flight 2 DMSP Satellite, AFGL-TR-78-0071, AD A058 503.
5. Meng, C.-I., Holzworth, R.H., and Akasofu, S.-I. (1977) Auroral circle-delineating the poleward boundary of the quiet auroral belt, J. Geophys. Res. 82:164.
6. Meng, C.-I. and Kroehl, H.W. (1977) Intense uniform precipitation of low-energy electrons over the polar cap, J. Geophys. Res. 82:2305.
7. Mizera, P.F. and Fennell, J.F. (1978) Satellite observations of polar, magnetotail lobe, and interplanetary electrons at low energies, Rev. Geophys. Space Phys. 16:147.
8. Foster, J.C. and Burrows, J.R. (1976) Electron fluxes over the polar cap, 1, intense keV fluxes during poststorm quieting, J. Geophys. Res. 81:6016.
9. Candidi, M., Kroehl, H.W., Kosinski, G., and Buhmann, R.W. (1978) DMSP-F2 observations of cusplike electron precipitation regions during the September 19-21, 1977 event, Space. Sci. Rev. 22:667.
10. Whalen, James A. (1970) Auroral Oval Plotter and Nomograph for Determining Corrected Geomagnetic Local Time, Latitude and Longitude for High Latitudes in the Northern Hemisphere, AFCRL-70-0422, AD 713 170.
11. Rossberg, L. (1978) Undisturbed trapping boundary for energetic electrons at low altitudes, J. Geophys. Res. 83:4307.

12. Huber, A., Pantazis, J., Besse, A.L., and Rothwell, P.L. (1977)  
Calibration of the SSJ/3 Sensor on the DMSP Satellites, AFGL-TR-77-0202, AD A045 977.
13. Archuleta, R.J. and DeForest, S.E. (1971) Efficiency of channel electron multipliers for electrons of 1-50 keV, Rev. of Sci. Instru. 42:89.
14. Lincoln, J. Virginia (1978) Geomagnetic and solar data, J. Geophys. Res. 83:232, 744.

Printed by  
United States Air Force  
Hanscom AFB, Mass. 01731